CMS Physics Analysis Summary

Contact: cms-pag-conveners-exotica@cern.ch 2020/05/04

Search for long-lived particles decaying into displaced jets

The CMS Collaboration

Abstract

An inclusive search for long-lived particles decaying into jets is presented. The search uses a data sample corresponding to an integrated luminosity of 132 fb^{-1} from proton-proton collisions at a center-of-mass energy of 13 TeV, collected with the CMS detector at the LHC in 2016, 2017, and 2018. The analysis examines the distinctive topology of displaced tracks and displaced vertices within a dijet system. For a simplified model, where pair-produced long-lived neutral particles decay into quark-antiquark pairs, pair production cross sections larger than 0.07 fb are excluded at 95% confidence level for long-lived particle masses larger than 500 GeV and mean proper decay lengths between 2 and 250 mm. For a model where the standard model Higgs boson decays to two long-lived scalars and then each scalar decays to a quark-antiquark pair, branching fractions larger than 1% can be excluded for mean proper decay lengths between 1 mm and 1 m. A group of supersymmetry models with pair-produced long-lived gluinos or top squarks decaying into different final-state topologies containing displaced jets is also tested. Gluino masses up to 2500 GeV and top squark masses up to 1600 GeV are excluded for mean proper decay lengths between 3 and 300 mm. The best mass bounds reach 2600 GeV for long-lived gluinos and 1800 GeV for long-lived top squarks. These are currently the most restrictive limits on these models.

1 Introduction

The existence of long-lived particles is a common feature in both the standard model (SM) and beyond the standard model (BSM) scenarios. The BSM physics cases for the production of long-lived particles at the CERN LHC are extremely rich. Examples include but are not limited to: split supersymmetry (SUSY) [1–7], where the gluino decays are suppressed by heavy scalars; SUSY with weak R-parity violation (RPV) [8–12], where the decays of the lightest supersymmetric particle (LSP) are suppressed by small RPV couplings; SUSY with gauge-mediated supersymmetry breaking (GMSB) [13–15], where the decays of the next-to-lightest supersymmetric particle (NLSP) are suppressed by a large SUSY-breaking scale; "stealth SUSY" [16, 17]; "Hidden Valley" models [18–20]; dark matter candidates [21–28]; heavy neutral leptons [29–32]; and neutral naturalness [33–37]. In the physics cases discussed above, it is quite common for the long-lived particles to further decay into final states containing jets, giving rise to displaced jets signatures.

Given the large variety of the BSM scenarios that lead to displaced jets signatures, it is important to make the displaced jets search as model-independent as possible. In this note, we present an inclusive search for long-lived particles decaying into jets, with at least one long-lived particle having a decay vertex displaced from the production vertex by up to around 55 cm in the transverse plane. Events used in this analysis were collected with the CMS detector [38] at the LHC from proton-proton (pp) collisions at a center-of-mass energy of 13 TeV in 2017 and 2018, corresponding to an integrated luminosity of 95.9 fb^{-1}, and the results are combined with a previous displaced jets search using the events collected in 2016 [39], accumulating into a total integrated luminosity of 132 fb^{-1}. The search looks for dijets formed by jets clustered from energy deposits in the calorimeters. For jets arising from the decay of a long-lived particle, the associated tracks are usually displaced from the primary vertices, and the decay vertex can be reconstructed from the displaced tracks. The properties of the tracks and the secondary vertex can provide discrimination power to distinguish long-lived signatures from the SM backgrounds. A large number of models predict long-lived particles decaying into displaced jets. Our tests for some of these will be discussed in detail in Section 3. Compared to the 2016 displaced jets search, a set of new techniques that significantly improves the sensitivity to long-lived signatures is implemented. Results of searches for similar long-lived particle signatures with hadronic decays at $\sqrt{s} = 13$ TeV have also been reported by ATLAS [40–44] and CMS [45–47].

2 The CMS detector

The central feature of the CMS apparatus is a superconducting solenoid of 6 m internal diameter, providing a magnetic field of 3.8 T. Within the solenoid volume are a silicon pixel and strip tracker, a lead tungstate crystal electromagnetic calorimeter (ECAL), and a brass and scintillator hadron calorimeter (HCAL), each composed of a barrel and two endcap detectors. Muons are detected in gas-ionization chambers embedded in the steel flux-return yoke outside the solenoid.

The silicon tracker measures charged particles within the pseudorapidity range $|\eta| < 2.5$. During the LHC run in 2017 and 2018, the silicon tracker consisted of 1856 silicon pixel and 15 148 silicon strip detector modules.

In the region $|\eta| < 1.74$, the HCAL cells have widths of 0.087 in pseudorapidity and 0.087 in azimuth. In the η-ϕ plane, and for $|\eta| < 1.48$, the HCAL cells map on to 5×5 arrays of ECAL crystals to form calorimeter towers projecting radially outward from the nominal interaction

point. For $|\eta| > 1.74$, the coverage of the towers increases progressively to a maximum of 0.174 in $\Delta\eta$ and $\Delta\phi$. Within each tower, the energy deposits in ECAL and HCAL cells are summed to define the calorimeter tower energies, and are subsequently used to provide the energies and directions of hadronic jets.

Events of interest are selected using a two-tiered trigger system [48]. The first level (L1), composed of custom hardware processors, uses information from the calorimeters and muon detectors to select events at a rate of around 100 kHz within a time interval of less than 4 μs. The second level, known as the high-level trigger (HLT), consists of a farm of processors running a version of the full event reconstruction software optimized for fast processing, and reduces the event rate to around 1 kHz before data storage.

A more detailed description of the CMS detector, together with a definition of the coordinate system used and the relevant kinematic variables, can be found in Ref. [38].

3 Data sets and simulated samples

Data were collected with two dedicated HLT displaced-jet triggers in 2017 and 2018. At the trigger level, jets are reconstructed from the energy deposits in the calorimeter towers, clustered using the anti-k_T algorithm [49, 50] with a distance parameter of 0.4. In this process, the contribution from each calorimeter tower is assigned a momentum, the absolute value and the direction of which are given by the energy measured in the tower and the coordinates of the tower. The raw jet energy is obtained from the sum of the tower energies, and the raw jet momentum from the vector sum of the tower momenta, which results in a nonzero jet mass. The raw jet energies are then corrected [51] to establish a uniform relative response of the calorimeter in η and a calibrated absolute response in transverse momentum p_T.

Events may contain multiple primary vertices, corresponding to multiple pp collisions occurring in the same bunch crossing. The reconstructed vertex with the largest value of summed physics-object p_T^2 is taken to be the primary pp interaction vertex, referred to as the leading primary vertex. The physics objects are the "jets," clustered using the jet finding algorithm [49, 50] with the tracks assigned to the vertex as inputs, and the associated missing transverse momentum, taken as the negative vector sum of the p_T of those jets. More details are given in Section 9.4.1 of Ref. [52].

The first displaced-jet trigger (referred to as the displaced trigger) requires an H_T larger than 430 GeV, where H_T is defined as the scalar sum of the transverse momenta of all jets satisfying $p_T > 40$ GeV and $|\eta| < 2.5$ in the event. The trigger also requires the presence of at least two jets, each of them satisfying the following requirements:

- $p_T > 40$ GeV and $|\eta| < 2.0$;
- at most two associated prompt tracks, which are tracks having a transverse impact parameter (IP_{2D}) with respect to the leading primary vertex smaller than 1.0 mm; and
- at least one associated displaced track, defined as a track with an IP_{2D} larger than 0.5 mm, and an impact parameter significance ($Sig[IP_{2D}]$) larger than 5.0, where the significance is the ratio of the impact parameter to its uncertainty.

The second displaced-jet trigger (referred to as the inclusive trigger) requires $H_T > 650$ GeV and the existence of at least two jets, each of them satisfying:

- $p_T > 60$ GeV and $|\eta| < 2.0$;

- at most two associated prompt tracks.

The displaced trigger has better efficiency for low-mass long-lived particles, while the inclusive trigger is designed to recover the trigger efficiency for high-mass long-lived particles with small ($<\sim 3$ mm) or large ($>\sim 300$ mm) mean proper decay length ($c\tau_0$).

The background sources of this search mainly arise from the SM events comprised of jets produced through the strong interaction, referred to as quantum chromodynamics (QCD) multijet events. The QCD multijet Monte Carlo (MC) sample is simulated with MADGRAPH5_*a*MC@NLO 2.2.2 [53] at leading order, which is interfaced with PYTHIA 8.212 [54] for parton showering, hadronization, and fragmentation. Jets from the matrix element calculations are matched to parton shower jets using the MLM algorithm [55]. The CP5 tune [56] is used for modeling the underlying event. For parton distribution function (PDF) modeling, the NNPDF3.1 PDF set [57] is used.

One of the benchmark signal models is a simplified model, referred to as the jet-jet model, where long-lived scalar neutral particles X are pair-produced through a $2 \to 2$ scattering process, mediated by an off-shell Z boson propagator. Each X particle decays to a quark-antiquark pair, and is assumed to do so with equal branching fractions to u, d, s, c, and b quark pairs. The chosen signature has two displaced vertices, each of which has a pair of associated jets. The samples are produced with different resonance masses ranging from 50 to 1500 GeV, and with different proper decay lengths ranging from 1 mm to 10 m.

Another signature we consider is the case where long-lived particles arise from exotic decays the SM Higgs boson, which can happen in many BSM scenarios (an excellent review can be found in the Section IV.6.6 of Ref. [58]), examples include "Hidden Valley" models [18, 19], Twin Higgs models [36], and the Folded SUSY model [59]. For the simulation, we use POWHEG [60–63] to produce 125 GeV Higgs events with gluon-gluon fusion production. The 125 GeV Higgs boson then decays to two long-lived scalars S, and each scalar then decays to a quark-antiquark pair. The samples are produced with the scalar mass m_S set to be 55 GeV, 40 GeV, or 15 GeV, while the $c\tau_0$ of the scalar varies from 1 mm to 3 m.

We also consider a group of SUSY models with different final state topologies. The first one is a GMSB SUSY model [64] in the general gauge mediation scenario [14, 15], where gluinos are pair produced, and the gravitino is the LSP whilst the gluino is the NLSP. After the gluino is produced, it forms an *R*-hadron, and then decays to a gluon and a gravitino, producing a displaced single jet and missing transverse momentum. This decay is suppressed by the SUSY-breaking scale, therefore the gluino is long-lived. This is referred to as the $\widetilde{g} \to g\widetilde{G}$ model. The samples are produced with gluino masses from 800 GeV to 2500 GeV, and with the $c\tau_0$ of the gluino varying from 1 mm to 10 m.

The second SUSY model we consider is a mini-split SUSY model [6, 7], where the gluino decays to a quark-antiquark pair and the lightest neutralino ($\widetilde{\chi}_1^0$), referred to as the $\widetilde{g} \to q\overline{q}\widetilde{\chi}_1^0$ model. This decay is mediated by a squark, which is much heavier than the gluino, therefore the decay is suppressed by the large scale characterizing the squark mass and the gluino is long-lived. The mass of the neutralino is assumed to be 100 GeV, the samples are produced with gluino masses from 1400 to 3000 GeV, and the $c\tau_0$ of the gluino varies from 1 mm to 10 m.

The third SUSY model is an RPV SUSY model [65] with minimum flavor violation, where the gluino is long lived and decays to a top quark and a top squark, the top squark is assumed to be virtual and decays to a strange antiquark and a bottom antiquark through the RPV interaction with strength given by the coupling λ''_{323} [12], effectively resulting in a three-body decay with a "multijet" final-state topology. This is referred to as the $\widetilde{g} \to tbs$ model. The samples are

produced with gluino masses from 1200 to 3000 GeV, and a $c\tau_0$ varying from 1 mm to 10 m.

We also considered a pair of RPV SUSY models [66] with semi-leptonic decays, in which the long-lived top squark decays to a bottom quark (down quark) and a charged lepton via an RPV interactions with strengths given by couplings λ'_{133}, λ'_{233}, and λ'_{333} (λ'_{131}, λ'_{231}, and λ'_{331}) [12], assuming the decay rate to each of the three lepton flavors (e, μ, and τ) to be equal, referred to as the $\widetilde{\mathrm{t}} \to \mathrm{b}\ell$ ($\widetilde{\mathrm{t}} \to \mathrm{d}\ell$) models. The samples are produced with different top squark masses from 600 to 2000 GeV, and a proper decay length varying from 1 mm to 10 m.

Finally we consider another SUSY model motivated by dynamical R-parity violation (dRPV) [67, 68], where the long-lived top squark decays to two down antiquarks via RPV interaction with strength given by a nonholomorphic RPV coupling η''_{311} [69], referred to as the $\widetilde{\mathrm{t}} \to \overline{\mathrm{d}}\,\overline{\mathrm{d}}$ model. The samples are produced with different top squark masses from 800 to 1800 GeV, and $c\tau_0$ varying from 1 mm to 10 m.

The Feynman diagrams for the signal models considered are summarized in Figure 1. All the signal samples are produced with PYTHIA 8.212, and NNPDF3.1 LO is used for PDF modeling. For underlying event modeling the CP2 tune is utilized. In the SUSY models, a long-lived gluino or top squark can form a hadronic state through strong interactions, an R-hadron [9, 70, 71], which is simulated with PYTHIA. The fraction of produced gluino hadronizing into a gluino-gluon state is assumed to be 0.1. The interactions of the R-hadron with matter were studied following the simulation described in Ref. [72], and were found to have negligible impact on this analysis, since they have very little impact on the track and vertex reconstruction.

Both the background and the signal events are processed with a GEANT4-based [73] simulation for the detailed CMS detector response. To take account of the effects of additional pp interactions within the same or nearby bunch crossings ("pileup"), additional minimum bias events are overlaid on the simulated events to match the pileup distribution observed in the data.

4 Event reconstruction and preselections

This search examines dijet candidates in a given event, which are objects that consist of two jets. The algorithms for the offline jet reconstruction and primary vertex selection are the same as those applied at the trigger level (as described in Section 3), except that the full offline information is used. After the trigger selection, if an event passes the displaced trigger, we require the event have offline $H_\mathrm{T} > 500$ GeV, and dijet candidates are formed from all possible pairs of jets in the event, with the jets satisfying $p_\mathrm{T} > 50$ GeV and pseudorapidity $|\eta| < 2.0$. On the other hand, if an event only passes the inclusive trigger, it is required to have offline $H_\mathrm{T} > 700$ GeV, and the dijet candidates are formed from all possible pairs of jets in the event, with the jets satisfying $p_\mathrm{T} > 80$ GeV and $|\eta| < 2.0$. These selections are chosen such that the online H_T and jet p_T requirements in the displaced-jet triggers reach full efficiency.

In this search, the track candidates are required to have transverse momenta $p_\mathrm{T} > 1$ GeV and to have high purity. The high-purity selection is based on track information (such as the normalized χ^2 of the track fit, the impact parameters, and the number of hits in different layers) to reduce the rate of the fake tracks, and the selection is optimized separately for each iteration of the tracking [74] so that it is efficient for selecting tracks with different displacements. More details of the high-purity selection can be found in Ref. [74]. The η and ϕ of a given track are determined by the direction of its momentum vector at the closest approach point to the leading primary vertex. For a given dijet candidate, we associate track candidates with each jet by requiring that $\Delta R < 0.5$, where $\Delta R = \sqrt{(\Delta\eta)^2 + (\Delta\phi)^2}$ is the angular distance between the jet

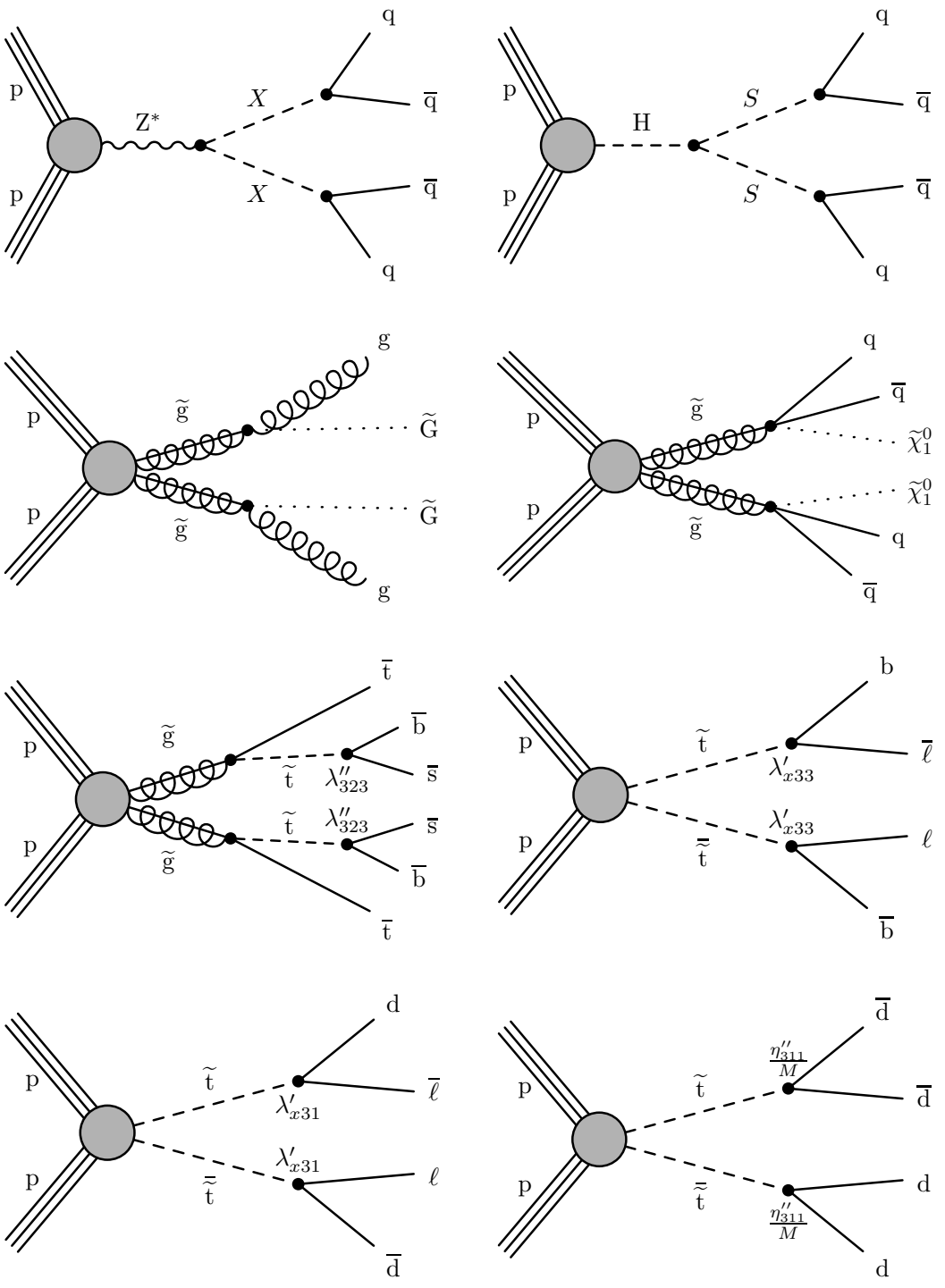

Figure 1: The Feynman diagrams for different long-lived models considered, including jet-jet model (upper left), exotic decay of the SM Higgs boson (upper right), general gauge mediation with $\widetilde{g} \to g\widetilde{G}$ decay (the second row, left), mini-split SUSY with $\widetilde{g} \to q\overline{q}\widetilde{\chi}_1^0$ decay (the second row, right), RPV SUSY with $\widetilde{g} \to tbs$ decay (the third row, left), RPV SUSY with $\widetilde{t} \to b\ell$ decay (the third row, right), RPV SUSY with $\widetilde{t} \to d\ell$ decay, and dynamical RPV SUSY with $\widetilde{t} \to \overline{d}\overline{d}$ decay (lower right).

axis and the track direction. When a track satisfies $\Delta R < 0.5$ for both jets, it is associated with the jet with smaller ΔR.

The next step is to reconstruct a secondary vertex for each dijet candidate. From all the tracks associated with a dijet candidate, we select displaced tracks that satisfy $\mathrm{IP_{2D}} > 0.5\,\mathrm{mm}$ and $\mathrm{Sig[IP_{2D}]} > 5.0$. We then attempt to reconstruct a secondary vertex from these displaced tracks using an adaptive vertex fitter algorithm [75]. To ensure the quality of the vertex reconstruction, only the secondary vertex with a χ^2 per degree-of-freedom ($\chi^2/\mathrm{n_{dof}}$) of less than 5.0 is selected. In order to suppress long-lived SM mesons and baryons, the invariant mass of the vertex is required to be larger than 4 GeV, and the transverse momentum of the vertex is required to be larger than 8 GeV, where the four-momentum of the vertex is calculated assuming the pion mass for all assigned tracks.

We only consider dijet candidates that have one reconstructed secondary vertex satisfying the above requirements. Furthermore, we select the track with the second-highest $\mathrm{Sig[IP_{2D}]}$ among the tracks that are assigned to the secondary vertex (the highest $\mathrm{Sig[IP_{2D}]}$ is usually more sensitive to the tail of impact parameter distribution in the background process, and is therefore less powerful). For displaced-jet signatures, where tracks tend to be more displaced, the two-dimensional IP significance of this selected track will be large. If it is smaller than 15, the dijet candidate is rejected. We also compute the ratio between the sum of energy for all the tracks assigned to the secondary vertex and the sum of the energy for all the tracks associated with the two jets. This ratio is expected to be large for displaced-jet signatures, therefore dijet candidates with a ratio smaller than 0.15 are rejected.

An additional variable, ζ, is defined to characterize the contribution of prompt activity to the jets. For each track associated with a jet, the primary vertex (including the leading primary vertex and the pileup vertices) with the minimum three-dimensional impact parameter significance to the track is identified. If this minimum three-dimensional impact parameter significance is smaller than 5, we assign the track to this primary vertex. Then for each jet, we compute the track energy contribution from each primary vertex, and the primary vertex with the largest track energy contribution to the jet is chosen. Finally, we define ζ as

$$\zeta = \frac{\sum_{\mathrm{track}\in \mathrm{PV}_1} E^{\mathrm{Jet}_1}_{\mathrm{track}} + \sum_{\mathrm{track}\in \mathrm{PV}_2} E^{\mathrm{Jet}_2}_{\mathrm{track}}}{E_{\mathrm{Jet}_1} + E_{\mathrm{Jet}_2}}, \tag{1}$$

which is the charged energy fraction of the dijet associated with the most compatible primary vertices. For displaced-jet signatures, ζ tends to be small since the jets are not compatible with primary vertices. Dijet candidates with ζ larger than 0.2 are rejected.

To help suppress the background events arising from nuclear interactions (NI) with the tracker material, we study the positions of the materials for the inner tracking system by reconstructing the NI vertex candidates. The NI vertices are also reconstructed using the adaptive vertex fitter, except that the events are collected with isolated single-muon triggers. The tracks used for the NI vertex reconstruction and the NI vertices themselves are required to satisfy the following criteria:

- For the track candidates utilized in the NI vertex reconstruction, we require that the tracks have $p_{\mathrm{T}} > 0.2\,\mathrm{GeV}$, high purity, $\mathrm{IP_{2D}} > 0.5\,\mathrm{mm}$, and $\mathrm{Sig[IP_{2D}]} > 5.0$. The tracks are also required to be associated with dijet candidates, for which the jets are required to have $p_{\mathrm{T}} > 10\,\mathrm{GeV}$, $|\eta| < 2.0$;
- vertex track multiplicity is larger than 3;
- vertex track energy fraction in the dijet is smaller than 0.15;

- vertex L_{xy} significance is larger than 200, where the transverse decay length L_{xy} is the distance between the secondary vertex and the leading primary vertex; and
- vertex $\chi^2/\mathrm{n_{dof}}$ is smaller than 3.0.

After these selections and noise subtractions, the distribution of the NI vertex candidates is transferred to a NI-veto map in the transverse plane, with $|x|(|y|) < 25\,\mathrm{cm}$, as shown in the Figure 2. For the noise subtraction, we only select the region where the NI vertex density is above a threshold that varies for different layers of the pixel detector. In the NI-veto map, we can clearly see the structures of the beam pipe (at $r \sim 2.3\,\mathrm{cm}$), the four pixel layers (at $r \sim 2.9$, ~ 6.8, ~ 10.9, and $\sim 16.0\,\mathrm{cm}$), and the support rails (at $r \sim 20\,\mathrm{cm}$). In our search, any secondary vertex candidate that overlaps with the NI-veto map is rejected. The loss of the fiducial volume within $r < 30\,\mathrm{cm}$ due to the veto is around 4%, and the efficiencies for signal events to pass this selection are generally well above 90%. Although in the veto we don't have selection on the z coordinates of the secondary vertices, we checked the impact on the signal efficiencies when restricting the veto to the barrel region of the pixel detector ($|z| < 27\,\mathrm{cm}$). That impact is found to be smaller than 0.1% and thus is negligible. A similar study on the structure of the CMS inner tracking system using a more dedicated nuclear interaction reconstruction technique with 2016 data has been reported in Ref. [76], the update of this study for the Phase I CMS pixel detector [77] will be public soon.

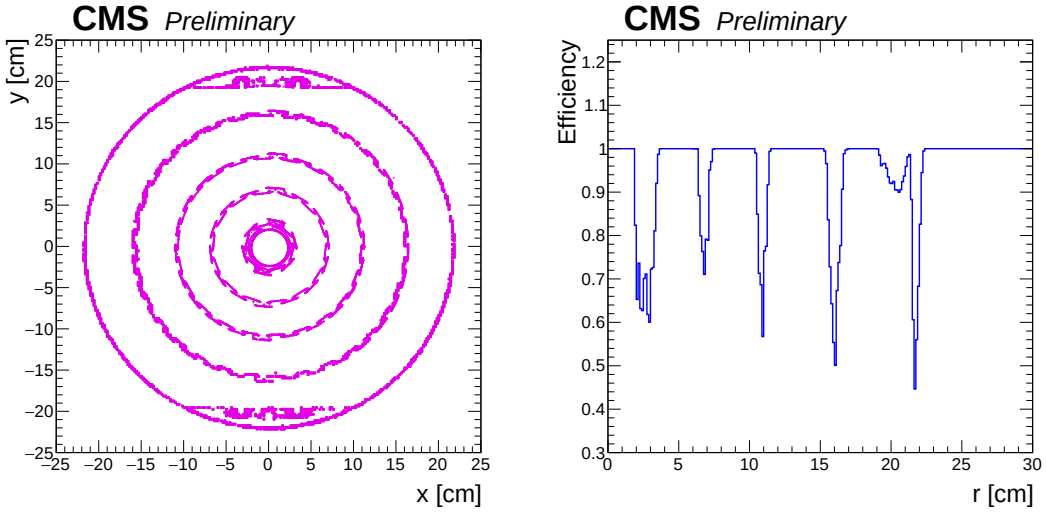

Figure 2: Left: the NI-veto map based on NI vertex reconstruction in the 2017 and 2018 data collected by the CMS detector, corresponding to the geometry of the Phase I CMS pixel detector [77]. The structures of different pixel layers can be clearly seen. Right: the efficiency for a given vertex candidate to pass the NI-veto as a function of radius r ($r = \sqrt{x^2 + y^2}$).

The preselection criteria for this search are summarized in Table 1, these preselection criteria are efficient for a wide range of long-lived models with different final-state topologies.

5 Event selection and background prediction

In addition to the secondary vertex reconstruction based on the adaptive vertex fitter, an auxiliary algorithm is employed to check the consistency between the secondary vertex system and the dijet system. For each displaced track (as defined in Section 3) associated with the dijet, an expected decay point consistent with the displaced dijet hypothesis is determined by finding the crossing point between the track helix and the dijet direction in the transverse plane. The

Table 1: Summary of the preselection criteria.

Secondary-vertex/dijet variable	Requirement
Vertex $\chi^2/\mathrm{n_{dof}}$	<5.0
Vertex invariant mass	$>4\,\mathrm{GeV}$
Vertex transverse momentum	$>8\,\mathrm{GeV}$
Second largest two-dimensional IP significance	>15
Vertex track energy fraction in the dijet	>0.15
ζ (charged energy fraction associated with compatible primary vertices)	<0.20
Vertex position in the x-y plane doesn't overlap with the NI-veto map.	

displaced tracks associated with the dijet are then clustered based on the expected transverse decay length (L_{xy}^{exp}) with respect to the leading primary vertex using a hierarchical clustering algorithm [78], in which two clusters are merged together when the smallest expected transverse decay length difference between the two clusters is smaller than 15% of the transverse decay length (L_{xy}) of the secondary vertex. When more than one cluster is formed after the final step of the hierarchical clustering, the one closest to the secondary vertex is selected. The cluster root-mean-square (RMS), which is a relative RMS of individual tracks L_{xy}^{exp} with respect to the secondary vertex L_{xy}, is computed to provide signal-background discrimination:

$$\mathrm{RMS_{cluster}} = \sqrt{\frac{1}{N_{\mathrm{tracks}}} \sum_{i=1}^{N_{\mathrm{tracks}}} \frac{(L_{xy}^{\mathrm{exp}}(i) - L_{xy})^2}{L_{xy}^2}}. \tag{2}$$

At the same time, for each track assigned to the secondary vertex, a sign is given to the $\mathrm{IP_{2D}}$ and $\mathrm{Sig[IP_{2D}]}$ based on the angle between the dijet direction and the impact parameter vector that points from the leading primary vertex to the closest approach point (with respect to the leading primary vertex) of the track in the transverse plane. The sign is positive if this angle is smaller than $\pi/2$, otherwise the sign is negative. A new variable, κ, is then introduced as the sum of the signed $\mathrm{Sig[IP_{2D}]}$ of the six leading tracks of the secondary vertex (where the tracks are ordered by the absolute values of their $\mathrm{Sig[IP_{2D}]}$):

$$\kappa = \sum_{i=1}^{6} \mathrm{Sig[IP_{2D}(track}_i\mathrm{)]}. \tag{3}$$

For background processes, since there is little underlying correlation between the secondary vertex system and the dijet system, the signed $\mathrm{Sig[IP_{2D}]}$ of different tracks tend to cancel each other, therefore κ will sharply peak around zero. On the other hand, for displaced jets that originate from the secondary vertex, the directions of the tracks will be highly correlated with the dijet direction, therefore the absolute value of κ tends to be large.

We then proceed to construct a multivariate discriminant based on the following variables for the vertex/dijet candidates:

- Vertex track multiplicity;
- Vertex L_{xy} significance;
- Cluster RMS;
- $|\kappa|$.

The distributions of the first three variables as well as κ are shown in Figure 3, with displaced-jet triggers, offline H_{T}, and offline jet kinematics selections applied. For the multivariate discriminant we utilize the Gradient Boosted Decision Trees (GBDT) [79–81], with cross entropy

as the loss function. Given the enormous cross section of the QCD process and the relatively low H_T threshold of our displaced-jet triggers, the statistics of the simulated QCD sample (after preselections) is insufficient for the training of the GBDT. Therefore for the background sample in the GBDT training, we use the data in the following region:

- Events are selected by the displaced-jet triggers, and pass the offline H_T and jet kinematics selections;
- the vertex track energy fraction in the dijet is smaller than 0.12 (therefore this region is orthogonal to the signal region);
- the veto using the NI-veto map is not applied;
- all the other preselection criteria are satisfied.

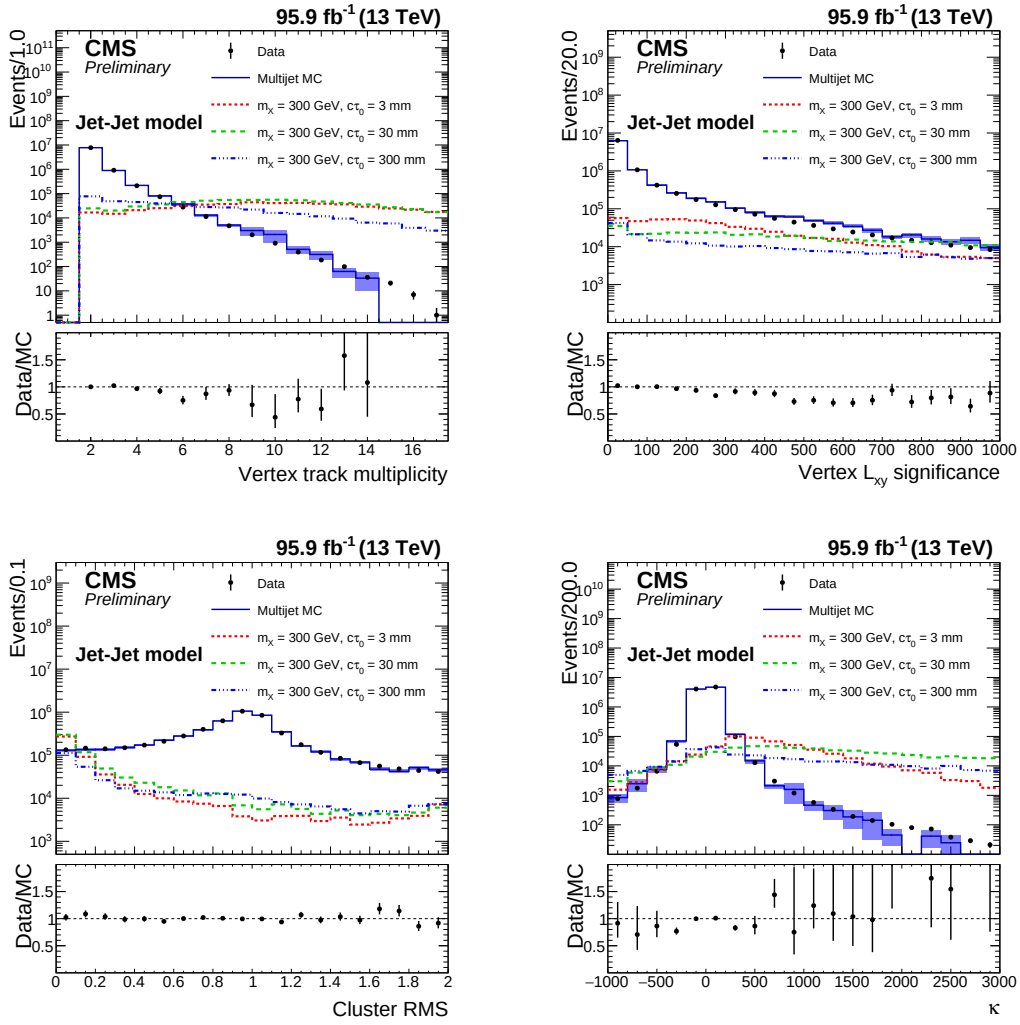

Figure 3: The distributions of the vertex track multiplicity (upper left), vertex L_{xy} significance (upper right), cluster RMS (lower left), and κ (lower right), for data, simulated QCD events, and simulated signal events. Data and simulated events are selected with the displaced-jet triggers, with the offline H_T, jets p_T, and η selections applied. The error bands and bars represent the statistical uncertainties. Three benchmark signal distributions are shown (dashed lines) for the jet-jet model with $m_X = 300\,\text{GeV}$ and varying $c\tau_0$. For visualization each signal process is given a cross section, σ, such that $\sigma \times 95.9\,\text{fb}^{-1} = 1 \times 10^6$.

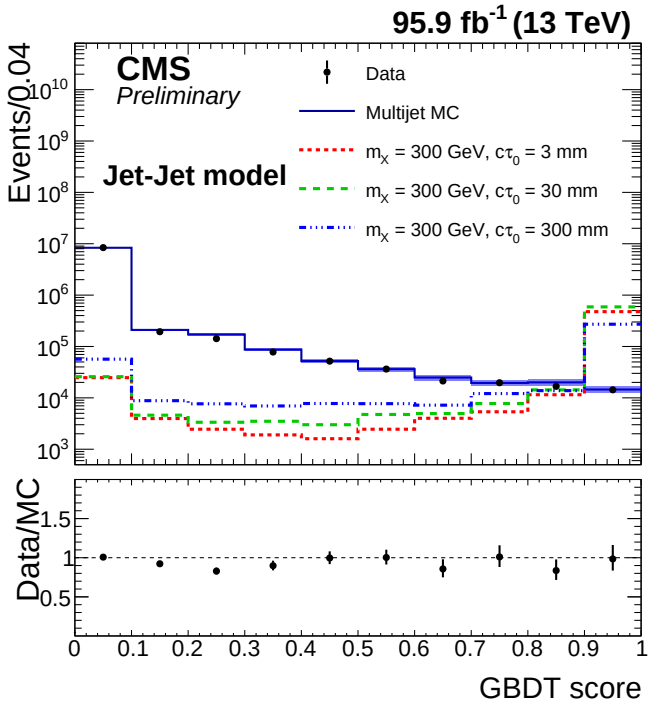

Figure 4: The distributions of the GBDT output for data, simulated QCD events, and simulated signal events. Data and simulated events are selected with the displaced-jet triggers, with the offline H_T, jets p_T, and η selections applied. The error bands and bars represent the statistical uncertainties. Three benchmark signal distributions are shown (dashed lines) for the jet-jet model with $m_X = 300\,\text{GeV}$ and varying $c\tau_0$. For visualization each signal process is given a cross section, σ, such that $\sigma \times 95.9\,\text{fb}^{-1} = 1 \times 10^6$. The signal events shown in this plot are not used in the GBDT training.

For the signal sample in the GBDT training, simulated jet-jet model events that pass preselection criteria are used, with $m_X = 100$, 300, and 1000 GeV, and with $c\tau_0 = 1$, 10, 100, 1000 mm. An event weight is assigned separately to each signal point such that the sum of weights is identical for each point. The GBDT algorithm is implemented using the TMVA (Toolkit for Multivariate Data Analysis) package [82] interfaced with Scikit-learn [83]. The GBDT scores for data, simulated QCD multijet events, and simulated signal events are shown in Figure 4. The signal efficiencies for this search will be measured with simulated signal events produced separately, and the background prediction is purely data-driven.

In addition to the GBDT score, we use another variable in the final event selection, which is the number of three-dimensional prompt tracks in a single jet, where the three-dimensional prompt tracks are the tracks that have three-dimensional impact parameters (IP_{3D}) with respect to the leading primary vertex smaller than 0.3 mm.

If more than one dijet candidate passes the preselection criteria described in Section 4, the one with the largest GBDT score is selected, if the GBDT scores are also the same, the one with the smallest $\chi^2/\text{n}_{\text{dof}}$ is selected. The candidate is then required to pass three final selection criteria, which are:

- Selection 1: for the leading jet, the number of three-dimensional prompt tracks is smaller than 3;

Table 2: The definition of the different regions used in the background estimation.

Region	Selection 1	Selection 2	Selection 3
A	Fail	Fail	Fail
B	Pass	Fail	Fail
C	Fail	Pass	Fail
D	Fail	Fail	Pass
E	Fail	Pass	Pass
F	Pass	Fail	Pass
G	Pass	Pass	Fail
H	Pass	Pass	Pass

- Selection 2: for the subleading jet, the number of three-dimensional prompt tracks is smaller than 3; and
- Selection 3: GBDT score g is larger than 0.988.

The numerical values for the selection criteria are chosen by optimizing the sensitivities to the jet-jet model across different X masses and lifetimes, with $m_X = 100$, 300, and 1000 GeV, and with $c\tau_0 = 1$, 10, 100, and 1000 mm.

The three selection criteria have small correlations for background processes, which is first verified with simulated QCD multijet events. Based on the three selection criteria, we can define eight non-overlapping regions A–H, as shown in Table 2. The region H is the region where the events pass all the three selection criteria, and thus is the signal region. Events in the remaining regions (A–G) fail one or more of the three selection criteria. Since the three selection criteria have little correlation between them for the background events, the background yield in the signal region H can be estimated by different ratios of event counts in regions A–G, where the ratio G(D+E+F)/(A+B+C) uses the fraction of events passing to those failing the likelihood discriminant selection (selection 3) and is taken as the central value of the predicted background yields. Three additional ratios are computed using the events failing either one of the first two selections:

- Cross-check 1: G(D+E)/(A+C);
- Cross-check 2: G(D+F)/(A+B);
- Cross-check 3: G(E+F)/(B+C).

These cross-checks provide an important test of the robustness of the background prediction and the assumption that the three selection criteria are minimally correlated. Differences between the predictions obtained with the nominal ratio G(D+E+F)/(A+B+C) and the cross-checks are also used to estimate the systematic uncertainty in the background prediction.

The method described above can be generalized to predict the background yield in arbitrary intervals of the GBDT score g, where the first two selections are also satisfied. In this way we can verify our background prediction method in the different bins of GBDT score g. The background prediction method is first tested with simulated QCD multijet events and simulated signal events, and is found to be robust both with and without signal contaminations. We then test the background prediction in data, for which we define a control region by inverting the selection on the vertex track energy fraction in the dijet, requiring this fraction to be smaller than 0.15. In order to improve the statistical precision we remove the veto using the NI-veto map. The predicted background yields and observed events in the control region are shown in Figure 5, where there is a good agreement between the predictions and the observations.

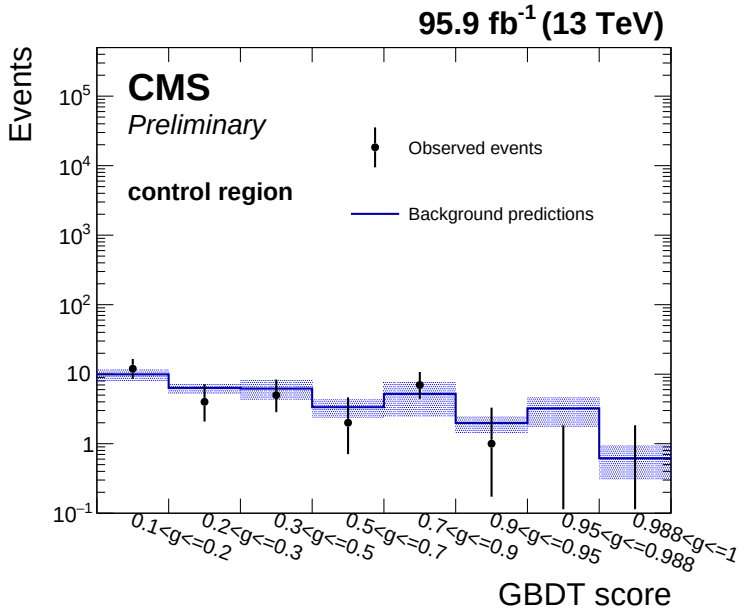

Figure 5: The predicted background yields and the observed events in the control region, for different bins of the GBDT scores. The error bands for the predictions represent statistical uncertainties and systematic uncertainties added in quadrature. The error bars for the observed events represent statistical uncertainties assuming Poisson statistics.

6 Systematic uncertainties

The systematic uncertainty in the background prediction is taken to be the largest deviation from the nominal prediction G(D+E+F)/(A+B+C) to the three cross-checks, and is found to be 52% in the final signal region where the GBDT score g is larger than 0.988.

The integrated luminosity systematic uncertainties for 13 TeV pp collision data are 2.3% and 2.5% for 2017 [84] and 2018 [85] data taking periods, respectively, and are applied as uncorrelated systematic uncertainties in signal yields.

The systematic uncertainty in signal yields due to the online H_{T} requirements of the displaced-jet triggers is estimated by comparing the efficiencies of the online H_{T} requirements in data and in MC simulations. The measurements are performed using the events collected with an isolated single-muon trigger. The discrepancies between the measurements in data and in MC simulations are parameterized as functions of offline H_{T}, and are applied to the simulated signal events. The signal yields are then recalculated for different masses and mean proper decay lengths. The largest correction in the signal yield for a given model is taken as the corresponding systematic uncertainty, and is found to be smaller than 2%.

The systematic uncertainty in signal yields due to the online jet p_{T} requirements of the displaced-jet triggers is estimated by measuring the per-jet efficiencies of the online jet p_{T} requirements in data and in MC simulations, using events collected with a prescaled H_{T} trigger that requires $H_{\mathrm{T}} > 425\,\mathrm{GeV}$. The discrepancies between the measurements in data and MC simulation are applied to simulated signal events, and the signal yields are recalculated. The correction is more significant for low-mass long-lived particles (with $m \sim 50\,\mathrm{GeV}$), and is smaller than 8%, which is taken as the corresponding systematic uncertainty.

To estimate the systematic uncertainty due to the online tracking requirements of the displaced-

jet triggers, we measure the per-jet efficiencies of the online tracking requirements as functions of the number of the prompt tracks and displaced tracks, using events collected with the prescaled H_T trigger. The efficiencies obtained in data are found to be consistent with or even larger than the efficiencies obtained in MC simulations. Therefore no corresponding systematic uncertainty is assigned.

To estimate the impact of the possible mismodeling of the GBDT score in MC simulation on signal yields, we compare the distribution of the GBDT score in simulated QCD multijet events with the distribution measured in data, using events collected with the prescaled H_T trigger. The discrepancies between data and MC simulation are taken account of by varying the GBDT scores in the simulated samples by the same magnitude. The largest variation in the signal efficiency for a given model is taken as the corresponding systematic uncertainty in signal yields, and is found to be 4%–15%.

Similarly, the uncertainty in signal yields due to impact parameter modeling is estimated by comparing the distribution of the impact parameters in simulated QCD multijet events with the distribution measured in data, also using events collected with the prescaled H_T trigger. The discrepancies between data and MC simulation are taken account of by varying the impact parameters in the simulated samples by the same magnitude. The largest variation in the signal efficiency for a given model is taken as the corresponding systematic uncertainty, and is found to be 8%–18%.

The impact of the jet energy scale uncertainty on the signal yields is estimated by varying the jet energy and p_T by one standard deviation of the jet energy scale uncertainty. The variations of the signal efficiencies are smaller than 3%, which is taken as the corresponding systematic uncertainty.

The impact of the PDF uncertainty on the signal yields is estimated by reweighting the simulated signal events with NNPDF, CT14 [86] and MMHT14 [87] PDF sets, and their associated uncertainty sets [88, 89]. The uncertainty in signal efficiencies for a given signal model is quantified by comparing the efficiencies calculated with alternative PDF sets and the ones with the nominal NNPDF set, and is found to be 4%–6%.

The uncertainty in signal yields due to the selection of the primary vertex is estimated by replacing the leading primary vertex with the subleading primary vertex when calculating impact parameters and vertex displacement. The largest variation of the signal efficiency for a given signal model is taken as the corresponding systematic uncertainty, and is found to be 8%–15%.

The systematic uncertainties in signal yields are summarized in Table 3 for different sources.

7 Results

7.1 Data in the signal region

After all preselection criteria are applied, the predicted background yields and the number of observed events in different GBDT ranges are shown in Figure 6, with number of three-dimensional prompt tracks smaller than 3 for both jets. The final signal region is the region where GBDT is larger than 0.988, and the predicted background yield is $0.75 \pm 0.44\,(\text{stat}) \pm 0.39\,(\text{syst})$.

Event yields in data after different selection requirements applied are shown in Table 4. We observe one event in the final signal region, which is consistent with the predicted background

Table 3: Summary of the systematic uncertainties in signal yields.

Source	Uncertainties (%)
Integrated luminosity	2.3 – 2.5
Online H_T requirement	0 – 2
Online jet p_T requirement	0 – 8
Offline vertexing	4 – 15
Track impact parameter modeling	8 – 18
Jet energy scale	0 – 3
PDF	4 – 6
Primary vertex selection	8 – 15
Total	17 – 25

yield. The observed event has an offline H_T of 570 GeV, and a secondary vertex candidate with a transverse decay length of around 26 cm and 8 assigned tracks. The position of the secondary vertex is close to one of the silicon strip layers, and was likely produced by nuclear interactions with the silicon strip detector.

Table 4: Event yields after different selection requirements applied for data collected in 2017 and 2018. Signal efficiencies for jet-jet model with $m_X = 1000$ GeV and different $c\tau_0$ are also shown for comparison.

Selections	Observed events in data	Signal efficiency ($m_X = 1000$ GeV) $c\tau_0$		
		3 mm	30 mm	300 mm
Displaced-jet triggers, offline H_T selections	17758640	69.4%	91.2%	80.5%
Offline jet p_T and η selections, vertex $\chi^2/n_{dof} < 5.0$	8387775	68.9%	90.7%	73.5%
Vertex $p_T > 8$ GeV	3794960	68.2%	90.3%	69.4%
Vertex invariant mass > 4 GeV	1129531	66.5%	89.3%	61.6%
Second largest Sig[IP_{2D}] > 15	422449	66.0%	89.0%	60.9%
Secondary vertex track energy fraction > 0.15	93873	64.3%	87.6%	58.4%
$\zeta < 0.20$	15891	63.6%	86.9%	57.9%
Veto using the NI-veto map	13721	63.6%	84.9%	55.4%
Number of 3D prompt tracks < 3 for each jet	2753	54.6%	76.4%	48.4%
GBDT > 0.988	1	51.5%	73.5%	42.5%

7.2 Interpretation of results

The signal yields in the final signal region are used to set limits on a variety of models. The signal efficiencies for representative signal points in different models can be found in Tables 5–13 and Figure 15 of Appendix A. The results obtained in this note are further combined with the results from the displaced jets search using the proton-proton collision data collected with the CMS experiment in 2016 [39], for which the systematic uncertainties arising from the same source are taken to be correlated, while the statistical uncertainties in signal yields or expected background yields are taken to be uncorrelated. The total integrated luminosity is 132 fb^{-1}.

Upper limits for a given model with different masses and lifetimes are presented by computing the 95% confidence level (CL) associated with each signal point according to the CL_s prescrip-

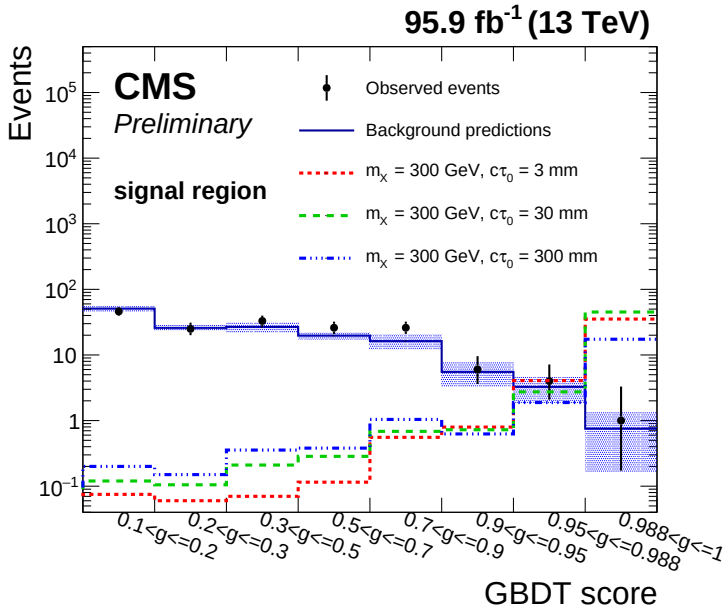

Figure 6: The predicted background yields and the number of observed events for the data in the signal region, with fewer than three 3D prompt tracks for both jets. The background predictions in different bins are correlated, since the events that are used for background predictions in lower bins are also used in the background predictions in higher bins. For comparison three benchmark signal points are also shown (dashed lines) for the jet-jet model with $m_X = 300\,\text{GeV}$ and varying lifetimes. For visualization, each signal process is given a cross section, σ, such that $\sigma \times L = 1 \times 10^2$.

tion [90–93], using an LHC-style profile likelihood ratio [92, 93] as the test statistic. The CL_s values are calculated using the asymptotic approximation [92], and have been verified with full-frequentist results for representative signal points.

Figure 7 presents the expected and observed upper limits (at 95% CL) on the pair production cross section for the jet-jet model at different scalar particle X masses and $c\tau_0$, assuming a 100% branching fraction. The limits are most stringent for $c\tau_0$ between 3 and 300 mm. For smaller $c\tau_0$, the limits become less restrictive because of the vetoes on prompt activity. Since the tracking efficiency decreases with larger displacement, the limits also become less stringent for larger $c\tau_0$ ($c\tau_0 > 300$ mm). Pair production cross sections larger than 0.07 fb are excluded at high mass ($m_X > 500$ GeV) for $c\tau_0$ between 2 and 250 mm. The lowest pair production cross section excluded is 0.04 fb, at $c\tau_0 = 30$ mm and with long-lived particle mass $m_X > 1000$ GeV.

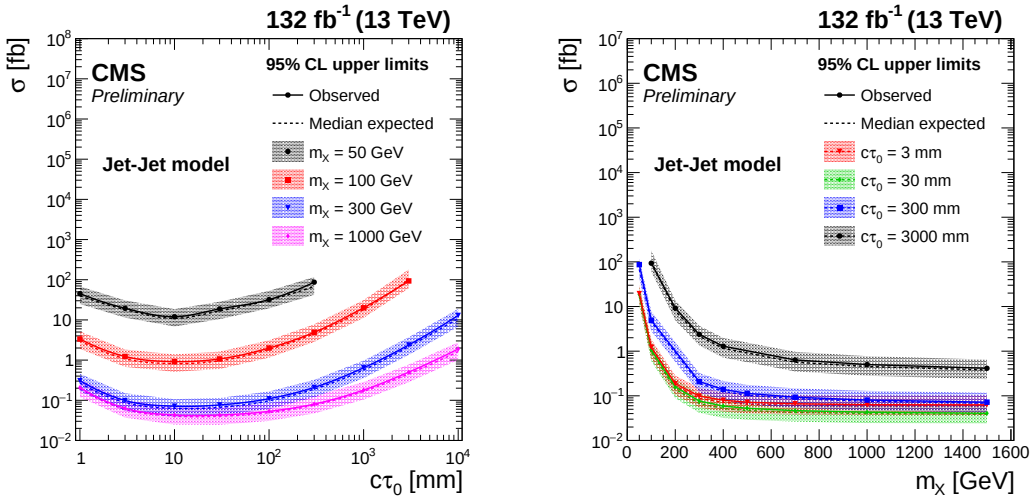

Figure 7: The expected and observed 95% CL upper limits on the pair production cross section of the long-lived particle X, assuming a 100% branching fraction for X to decay to a quark-antiquark pair, shown at different particle X masses and $c\tau_0$ for the jet-jet model. The solid (dashed) lines represent the observed (median expected) limits. The shaded bands represent the regions containing 68% of the distributions of the expected limits under the background-only hypothesis. The left plot shows the upper limits as a function of $c\tau_0$ for different masses, while the right plot shows the upper limits as a function of the particle mass for different $c\tau_0$.

Figure 8 presents the expected and observed upper limits (at 95% CL) on the branching fraction of the SM Higgs boson to decay to two long-lived scalars S, each of which decays to a quark-antiquark pair. The gluon-gluon fusion production cross section of the SM Higgs boson at 13 TeV [58] is assumed to calculate the upper limits on the branching fraction. When the long-lived scalar decays to a light-flavor quark-antiquark pair, branching fractions larger than 1% are excluded for $c\tau_0$ between 1 mm and 1 m with $m_S = 40, 55$ GeV. When the long-lived scalar decays to a bottom quark-antiquark pair, branching fractions larger than 10% are excluded for $c\tau_0$ between 1 mm and 1 m. These are the most stringent limits to date on this model for $c\tau_0$ between 1 mm and 1 m. For $m_S = 15$ GeV, where the track multiplicity of the secondary vertex is small, and the tracks are collimated, the limits become worse. The limits are also worse for the case where the scalar decays to a bottom quark-antiquark pair, because the decays of b-hadrons can produce tertiary vertices, which can be missed by the secondary vertex reconstruction we deploy in this search.

Figure 9 presents the expected and observed upper limits on the pair production cross section

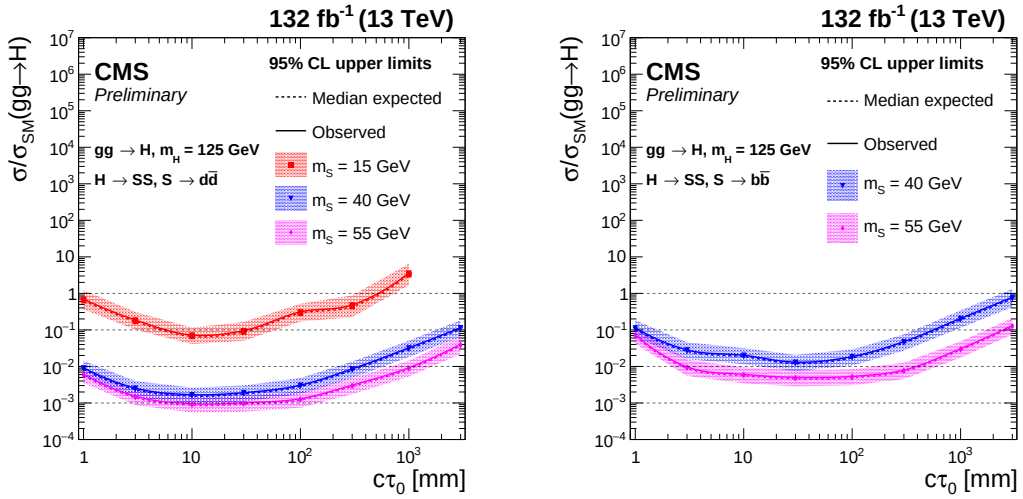

Figure 8: The expected and observed 95% CL upper limits on the branching fraction of the SM Higgs boson to decay to two long-lived scalars, assuming the gluon-gluon fusion SM Higgs production cross section of 49 pb at 13 TeV with $m_{\mathrm{H}} = 125\,\mathrm{GeV}$, shown at different masses and $c\tau_0$ for the scalar S. The solid (dashed) lines represent the observed (median expected) limits. The shaded bands represent the regions containing 68% of the distributions of the expected limits under the background-only hypothesis. The left plot shows the upper limits when each scalar decays to a down quark-antiquark pair, while the right plot shows the upper limits when each scalar decays to a bottom quark-antiquark pair.

of long-lived gluinos in the GMSB $\tilde{\mathrm{g}} \to \mathrm{g}\tilde{\mathrm{G}}$ model, assuming a 100% branching fraction for the gluino to decay into a gluon and a gravitino. Although in the $\tilde{\mathrm{g}} \to \mathrm{g}\tilde{\mathrm{G}}$ signature each displaced vertex is associated with only one jet, the two separate displaced single jets can be paired together and pass the selections, therefore the analysis is sensitive to this kind of signature. When the gluino mass is 2400 GeV, signal efficiencies are around 21%, 53%, and 41% in 2017 and 2018 for $c\tau_0 = 3$, 30, and 300 mm, respectively; and gluino pair production cross sections larger than 0.1 fb are excluded for $c\tau_0$ between 7 and 600 mm. The upper limits on the pair production cross section are then translated into upper limits on the gluino mass for different $c\tau_0$, based on a calculation at the next-to-next-to-leading logarithmic accuracy matched to the approximated next-to-next-to-leading order predictions ($\mathrm{NNLO_{approx}}$+NNLL) of the gluino pair production cross section at $\sqrt{s} = 13\,\mathrm{TeV}$ [94–99] in the limit where all the other SUSY particles are much heavier and decoupled. Gluino masses up to 2450 GeV are excluded for $c\tau_0$ between 6 and 550 mm. The largest gluino mass excluded is 2560 GeV with a $c\tau_0$ of 30 mm. The bounds are the most stringent to date on this model for $c\tau_0$ between 1 mm and 1 m.

Figure 10 shows the expected and observed upper limits on the pair production cross section of the long-lived gluinos in the mini-split $\tilde{\mathrm{g}} \to \mathrm{q}\bar{\mathrm{q}}\tilde{\chi}_1^0$ model, assuming a 100% branching fraction for the gluino to decay into a quark-antiquark pair and the lightest neutralino. The neutralino mass is assumed to be 100 GeV. When the gluino mass is 2400 GeV, signal efficiencies are around 31%, 69%, and 51% in 2017 and 2018 for $c\tau_0 = 3$, 30, and 300 mm, respectively; and gluino pair production cross sections larger than 0.1 fb are excluded for proper decay lengths between 3 and 900 mm. The upper limits on the pair production cross sections are then translated into upper limits on the gluino mass for different $c\tau_0$, based on the $\mathrm{NNLO_{approx}}$+NNLL gluino pair production cross sections. Gluino masses up to 2500 GeV are excluded for $c\tau_0$ between 5 and 520 mm. The largest gluino mass excluded is 2610 GeV with a $c\tau_0$ of 30 mm. The bounds are the most stringent to date on this model in the tested lifetime range.

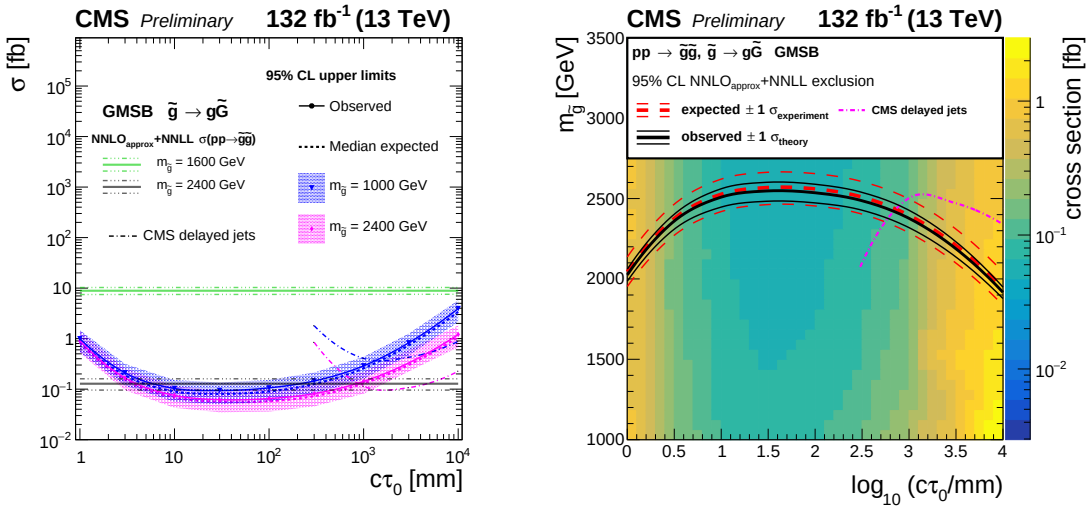

Figure 9: Left: the expected and observed 95% CL upper limits on the pair production cross section of the long-lived gluinos, assuming a 100% branching fraction for $\widetilde{g} \to g\widetilde{G}$ decays. The horizontal lines indicate the $\mathrm{NNLO_{approx}}$+NNLL gluino pair production cross sections for $m_{\widetilde{g}} = 2400\,\mathrm{GeV}$ and $m_{\widetilde{g}} = 1600\,\mathrm{GeV}$, as well as their variations due to the uncertainties in the choices of renormalization scales, factorization scales, and PDF sets. The solid (dashed) lines represent the observed (median expected) limits, the bands show the regions containing 68% of the distributions of the expected limits under the background-only hypothesis. The observed limits from the CMS search utilizing the timing capabilities of the ECAL system [47] are also shown for comparison. Right: the expected and observed 95% CL limits for the long-lived gluino model in the mass-lifetime plane, assuming a 100% branching fraction for $\widetilde{g} \to g\widetilde{G}$ decays, based on the $\mathrm{NNLO_{approx}}$+NNLL calculation of the gluino pair production cross section at $\sqrt{s} = 13\,\mathrm{TeV}$. The thick solid black (dashed red) line represents the observed (median expected) limits at 95% CL. The thin red lines indicate the region containing 68% of the distribution of the expected limits under the background-only hypothesis. The thin black lines represent the change in the observed limit due to the variation of the signal cross sections within the theoretical uncertainties.

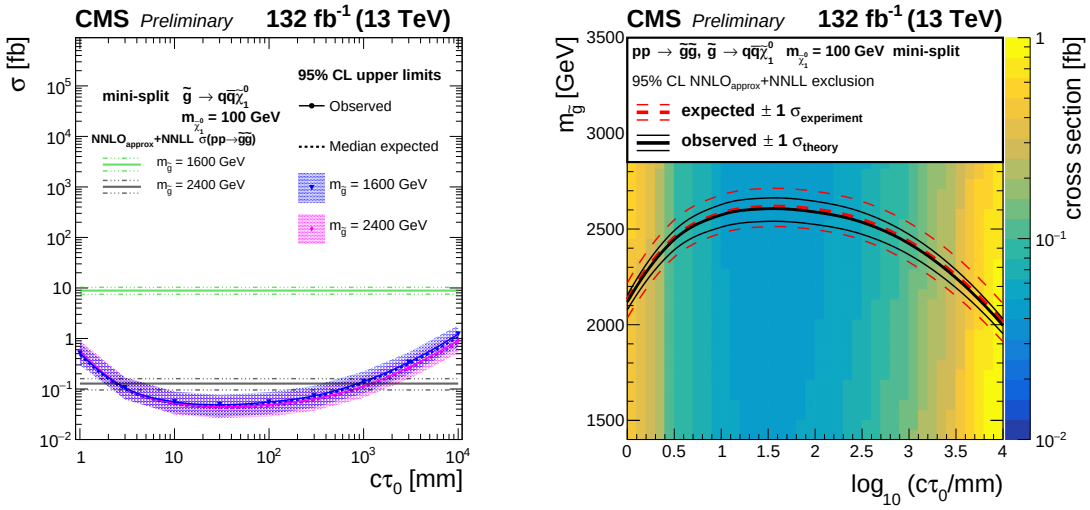

Figure 10: Left: the expected and observed 95% CL upper limits on the pair production cross section of the long-lived gluinos, assuming a 100% branching fraction for $\tilde{g} \to q\bar{q}\tilde{\chi}_1^0$ decays. The horizontal lines indicate the $\text{NNLO}_{\text{approx}}$+NNLL gluino pair production cross sections for $m_{\tilde{g}} = 2400\,\text{GeV}$ and $m_{\tilde{g}} = 1600\,\text{GeV}$, as well as their variations due to the uncertainties in the choices of renormalization scales, factorization scales, and PDF sets. The solid (dashed) lines represent the observed (median expected) limits, the bands show the regions containing 68% of the distributions of the expected limits under the background-only hypothesis. Right: the expected and observed 95% CL limits for the long-lived gluino model in the mass-lifetime plane, assuming a 100% branching fraction for $\tilde{g} \to q\bar{q}\tilde{\chi}_1^0$ decays, based on the $\text{NNLO}_{\text{approx}}$+NNLL calculation of the gluino pair production cross section at $\sqrt{s} = 13\,\text{TeV}$. The thick solid black (dashed red) line represents the observed (median expected) limits at 95% CL. The thin red lines indicate the region containing 68% of the distribution of the expected limits under the background-only hypothesis. The thin black lines represent the change in the observed limit due to the variation of the signal cross sections within the theoretical uncertainties.

Figure 11 presents the expected and observed upper limits on the pair production cross section of the long-lived gluinos in the $\widetilde{g} \to tbs$ model, assuming a 100% branching fraction for the gluino to decay into top, bottom, and strange quarks. When the gluino mass is 2400 GeV, signal efficiencies are around 41%, 81%, and 66% in 2017 and 2018 for $c\tau_0 = 3$, 30, and 300 mm, respectively; and gluino pair production cross sections larger than 0.1 fb are excluded for $c\tau_0$ between 3 and 1490 mm. The upper limits on the pair production cross sections are then translated into upper limits on the gluino mass for different $c\tau_0$, based on the NNLO$_{\text{approx}}$+NNLL gluino pair production cross sections. Gluino masses up to 2500 GeV are excluded for $c\tau_0$ between 3 and 1000 mm. The largest gluino mass excluded is 2640 GeV with a $c\tau_0$ of 30 mm. The bounds are the most stringent to date on this model in the tested lifetime range.

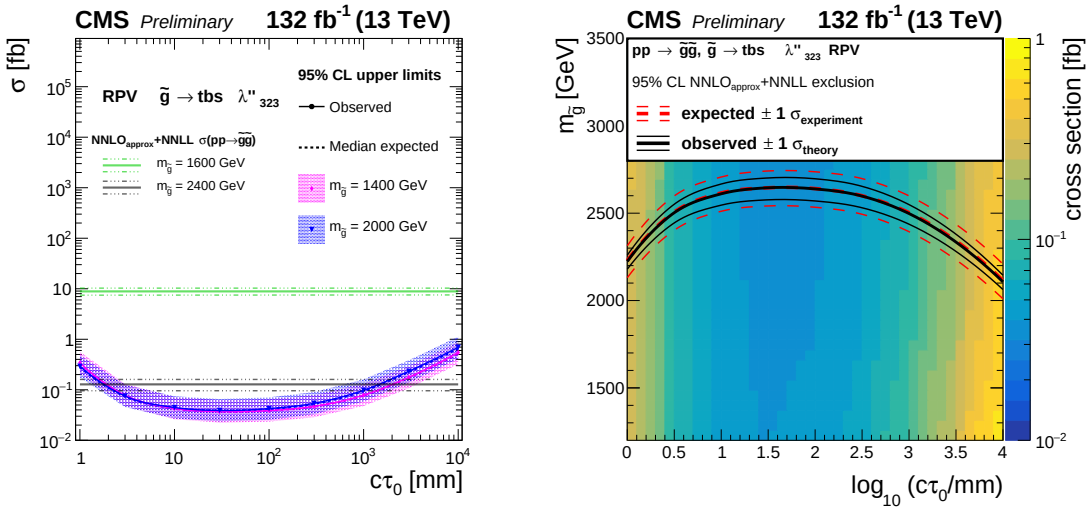

Figure 11: Left: the expected and observed 95% CL upper limits on the pair production cross section of the long-lived gluinos, assuming a 100% branching fraction for $\widetilde{g} \to tbs$ decays. The horizontal lines indicate the NNLO$_{\text{approx}}$+NNLL gluino pair production cross sections for $m_{\widetilde{g}} = 2400$ GeV and $m_{\widetilde{g}} = 1600$ GeV, as well as their variations due to the uncertainties in the choices of renormalization scales, factorization scales, and PDF sets. The solid (dashed) lines represent the observed (median expected) limits, the bands show the regions containing 68% of the distributions of the expected limits under the background-only hypothesis. Right: the expected and observed 95% CL limits for the long-lived gluino model in the mass-lifetime plane, assuming a 100% branching fraction for $\widetilde{g} \to tbs$ decays, based on the NNLO$_{\text{approx}}$+NNLL calculation of the gluino pair production cross section at $\sqrt{s} = 13$ TeV. The thick solid black (dashed red) line represents the observed (median expected) limits at 95% CL. The thin red lines indicate the region containing 68% of the distribution of the expected limits under the background-only hypothesis. The thin black lines represent the change in the observed limit due to the variation of the signal cross sections within the theoretical uncertainties.

Figure 12 shows the expected and observed upper limits on the pair production cross section of the long-lived top squarks in the RPV $\widetilde{t} \to b\ell$ model, assuming a 100% branching fraction for the top squark to decay into a bottom quark and a charged lepton, with equal branching fractions for e, μ, and τ. When the top squark mass is 1600 GeV, signal efficiencies are around 22%, 43%, and 26% in 2017 and 2018 for $c\tau_0 = 3$, 30, and 300 mm, respectively; and top squark pair production cross sections larger than 0.1 fb are excluded for $c\tau_0$ between 8 and 160 mm. The upper limits on the pair production cross sections are translated into upper limits on the top squark mass for different $c\tau_0$, based on the NNLO$_{\text{approx}}$+NNLL top squark pair production cross sections. Top squark masses up to 1600 GeV are excluded for $c\tau_0$ between 3 and 340 mm.

The largest top squark mass excluded is 1720 GeV with a $c\tau_0$ of 30 mm. The bounds are the most stringent to date on this model in the tested lifetime range.

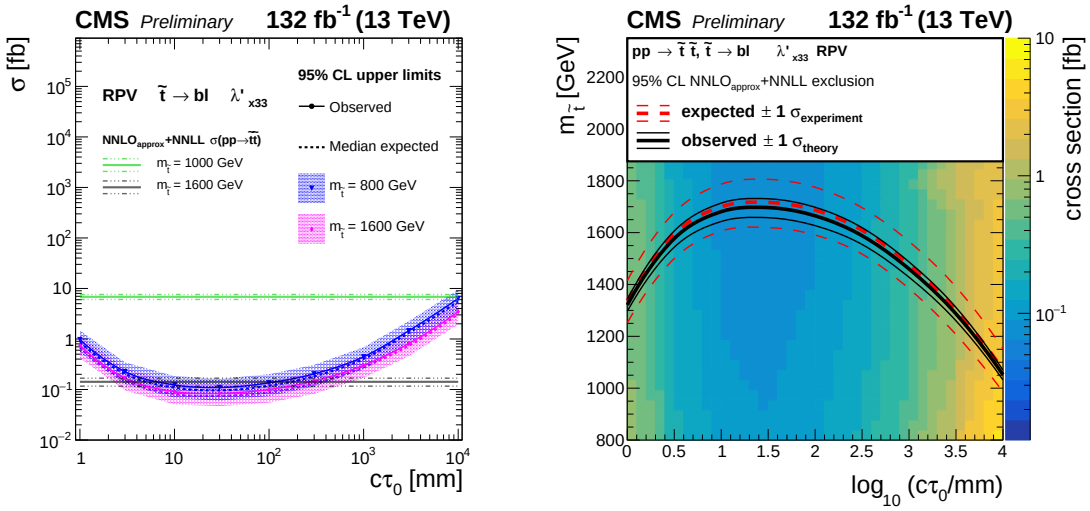

Figure 12: Left: the expected and observed 95% CL upper limits on the pair production cross section of the long-lived top squarks, assuming a 100% branching fraction for $\tilde{t} \to b\ell$ decays, with equal branching fractions for e, μ, and τ. The horizontal lines indicate the NNLO$_{\text{approx}}$+NNLL top squark pair production cross sections for $m_{\tilde{t}} = 1600$ GeV and $m_{\tilde{t}} = 1000$ GeV, as well as their variations due to the uncertainties in the choices of renormalization scales, factorization scales, and PDF sets. The solid (dashed) lines represent the observed (median expected) limits, the bands show the regions containing 68% of the distributions of the expected limits under the background-only hypothesis. Right: the expected and observed 95% CL limits for the long-lived top squark model in the mass-lifetime plane, assuming a 100% branching fraction for $\tilde{t} \to b\ell$ decays, based on the NNLO$_{\text{approx}}$+NNLL calculation of the top squark pair production cross section at $\sqrt{s} = 13$ TeV. The thick solid black (dashed red) line represents the observed (median expected) limits at 95% CL. The thin red lines indicate the region containing 68% of the distribution of the expected limits under the background-only hypothesis. The thin black lines represent the change in the observed limit due to the variation of the signal cross sections within the theoretical uncertainties.

Figure 13 shows the expected and observed upper limits on the pair production cross section of the long-lived top squarks in the RPV $\tilde{t} \to d\ell$ model, assuming a 100% branching fraction for the top squark to decay into a down quark and a charged lepton, with equal branching fractions for e, μ, and τ. When the top squark mass is 1600 GeV, signal efficiencies are around 25%, 48%, and 29% in 2017 and 2018 for $c\tau_0 = 3$, 30, and 300 mm, respectively; and top squark pair production cross sections larger than 0.1 fb are excluded for $c\tau_0$ between 7 and 220 mm. The upper limits on the pair production cross sections are translated into upper limits on the top squark mass for different $c\tau_0$, based on the NNLO$_{\text{approx}}$+NNLL top squark pair production cross sections. Top squark masses up to 1600 GeV are excluded for $c\tau_0$ between 3 and 430 mm. The largest top squark mass excluded is 1740 GeV with a $c\tau_0$ of 30 mm. The bounds are the most stringent to date on this model in the tested lifetime range.

Figure 14 shows the expected and observed upper limits on the pair production cross section of the long-lived top squarks in the dynamical-RPV $\tilde{t} \to \bar{d}\bar{d}$ model, assuming a 100% branching fraction for the top squark to decay into two down antiquarks. When the top squark mass is 1600 GeV, signal efficiencies are around 43%, 76%, and 53% in 2017 and 2018 for $c\tau_0 = 3$, 30, and 300 mm, respectively; and top squark pair production cross sections larger than 0.1 fb

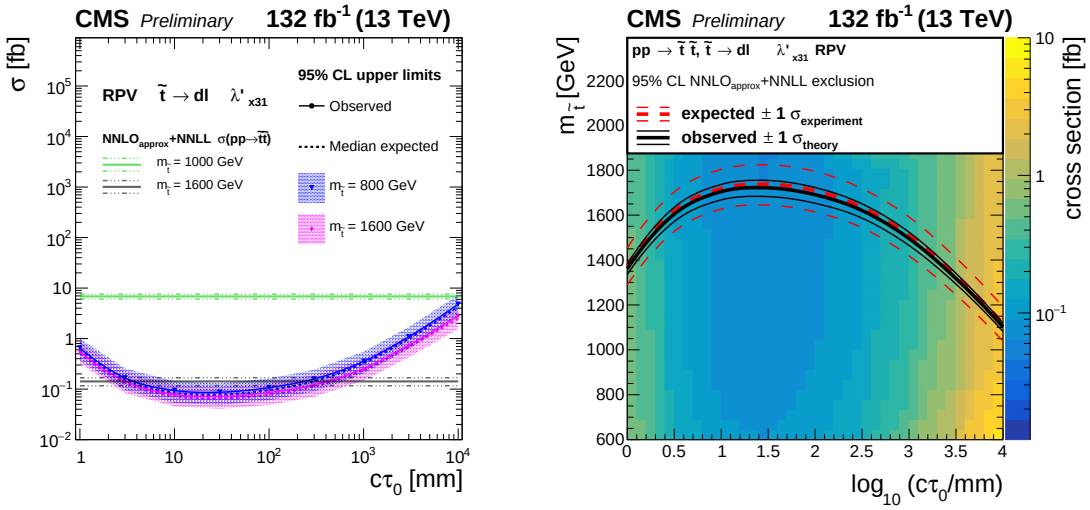

Figure 13: Left: the expected and observed 95% CL upper limits on the pair production cross section of the long-lived top squarks, assuming a 100% branching fraction for $\tilde{\mathrm{t}} \to \mathrm{d}\ell$ decays, with equal branching fractions for e, μ, and τ. The horizontal lines indicate the $\mathrm{NNLO_{approx}}$+NNLL top squark pair production cross sections for $m_{\tilde{\mathrm{t}}} = 1600\,\mathrm{GeV}$ and $m_{\tilde{\mathrm{t}}} = 1000\,\mathrm{GeV}$, as well as their variations due to the uncertainties in the choices of renormalization scales, factorization scales, and PDF sets. The solid (dashed) lines represent the observed (median expected) limits, the bands show the regions containing 68% of the distributions of the expected limits under the background-only hypothesis. Right: the expected and observed 95% CL limits for the long-lived top squark model in the mass-lifetime plane, assuming a 100% branching fraction for $\tilde{\mathrm{t}} \to \mathrm{d}\ell$ decays, based on the $\mathrm{NNLO_{approx}}$+NNLL calculation of the top squark pair production cross section at $\sqrt{s} = 13\,\mathrm{TeV}$. The thick solid black (dashed red) line represents the observed (median expected) limits at 95% CL. The thin red lines indicate the region containing 68% of the distribution of the expected limits under the background-only hypothesis. The thin black lines represent the change in the observed limit due to the variation of the signal cross sections within the theoretical uncertainties.

are excluded for $c\tau_0$ between 3 and 820 mm. The upper limits on the pair production cross sections are translated into upper limits on the top squark mass for different $c\tau_0$, based on the NNLO$_{\text{approx}}$+NNLL top squark pair production cross sections. Top squark masses up to 1600 GeV are excluded for $c\tau_0$ between 2 and 1320 mm. The largest top squark mass excluded is 1820 GeV with a $c\tau_0$ of 30 mm. The bounds are the most stringent to date on this model in the tested lifetime range.

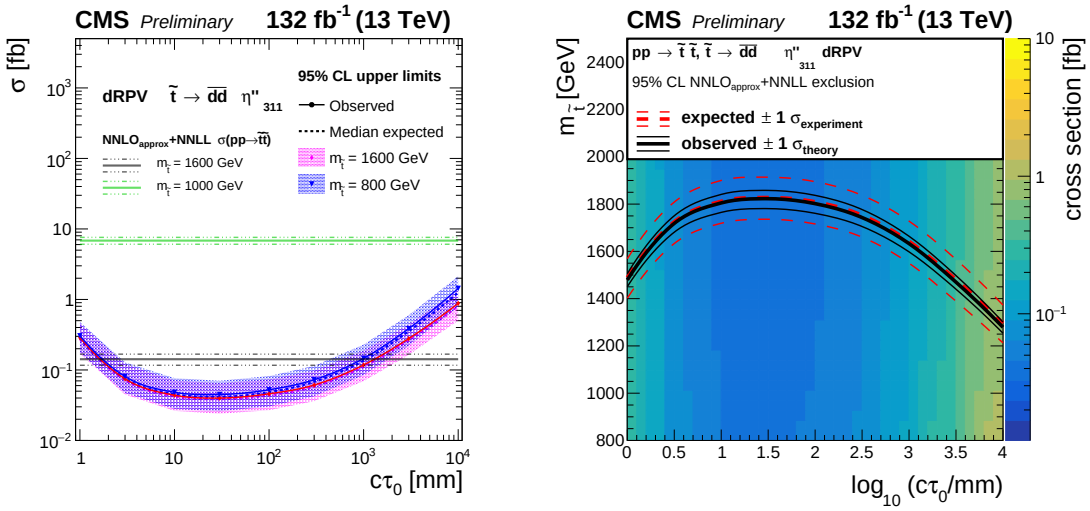

Figure 14: Left: the expected and observed 95% CL upper limits on the pair production cross section of the long-lived top squarks, assuming a 100% branching fraction for $\tilde{t} \to \bar{d}\bar{d}$ decays. The horizontal lines indicate the NNLO$_{\text{approx}}$+NNLL top squark pair production cross sections for $m_{\tilde{t}} = 1600$ GeV and $m_{\tilde{t}} = 1000$ GeV, as well as their variations due to the uncertainties in the choices of renormalization scales, factorization scales, and PDF sets. The solid (dashed) lines represent the observed (median expected) limits, the bands show the regions containing 68% of the distributions of the expected limits under the background-only hypothesis. Right: the expected and observed 95% CL limits for the long-lived top squark model in the mass-lifetime plane, assuming a 100% branching fraction for $\tilde{t} \to \bar{d}\bar{d}$ decays, based on the NNLO$_{\text{approx}}$+NNLL calculation of the top squark pair production cross section at $\sqrt{s} = 13$ TeV. The thick solid black (dashed red) line represents the observed (median expected) limits at 95% CL. The thin red lines indicate the region containing 68% of the distribution of the expected limits under the background-only hypothesis. The thin black lines represent the change in the observed limit due to the variation of the signal cross sections within the theoretical uncertainties.

8 Summary

We present a search for long-lived particles decaying to jets, using proton-proton collision data collected with the CMS experiment at a center-of-mass energy of 13 TeV in 2017 and 2018. The results are combined with a previous CMS search for displaced jets search using proton-proton collision data in 2016, accumulating to a total integrated luminosity of 132 fb^{-1}. After all selections, we observe one event in the data collected in 2017 and 2018, which is consistent with the predicted background yield. We set the best current limits on a variety of models with long-lived particles having mean proper decay lengths between 1 mm and 10 m. For a simplified model where pair-produced long-lived neutral particles decay to quark-antiquark pairs, pair production cross sections larger than 0.07 fb are excluded at 95% confidence level for mean

proper decay lengths between 2 and 250 mm at high mass ($m_X > 500$ GeV). For a model where the SM Higgs boson decays to two long-lived scalars and each long-lived scalar decays to a quark-antiquark pair, the branching fractions for the exotic Higgs decay larger than 1% are excluded at 95% confidence level for mean proper decay lengths between 1 mm and 1 m when scalar mass is 40 or 55 GeV. For a supersymmetric (SUSY) model in the general gauge mediation scenario, where the long-lived gluino decays to a gluon and a lightest SUSY particle, gluino masses up to 2450 GeV are excluded at 95% confidence level for mean proper decay lengths between 6 and 550 mm. For another SUSY model in the mini-split scenario, where the long-lived gluino can decay to a quark-antiquark pair and the lightest neutralino, gluino masses up to 2500 GeV are excluded at 95% confidence level for mean proper decay lengths between 7 and 360 mm. An *R*-parity violating (RPV) SUSY model is also tested, where the long-lived gluino can decay to top, bottom, and strange antiquarks, and gluino masses up to 2500 GeV are excluded at 95% confidence level for mean proper decay lengths between 3 and 1000 mm. We also study another RPV SUSY model, where the long-lived top squark can decay to a bottom quark and a charged lepton, and top squark masses up to 1600 GeV are excluded at 95% confidence level for mean proper decay lengths between 5 and 240 mm. For an RPV SUSY model, where the long-lived top squark can decay to a down quark and a charged lepton, top squark masses up to 1600 GeV are excluded at 95% confidence level for mean proper decay lengths between 3 and 360 mm. Finally, for a dynamical-RPV SUSY model, where the long-lived top squark can decay to two down antiquarks, top squark masses up to 1600 GeV are excluded at 95% confidence level for mean proper decay lengths between 2 and 1320 mm. These are the most stringent limits to date on these models.

References

[1] N. Arkani-Hamed and S. Dimopoulos, "Supersymmetric unification without low energy supersymmetry and signatures for fine-tuning at the LHC", *JHEP* **06** (2005) 073, doi:10.1088/1126-6708/2005/06/073, arXiv:hep-th/0405159.

[2] G. F. Giudice and A. Romanino, "Split supersymmetry", *Nucl. Phys. B* **699** (2004) 65, doi:10.1016/j.nuclphysb.2004.08.001, arXiv:hep-ph/0406088. [Erratum: doi:10.1016/j.nuclphysb.2004.11.048].

[3] J. L. Hewett, B. Lillie, M. Masip, and T. G. Rizzo, "Signatures of long-lived gluinos in split supersymmetry", *JHEP* **09** (2004) 070, doi:10.1088/1126-6708/2004/09/070, arXiv:hep-ph/0408248.

[4] N. Arkani-Hamed, S. Dimopoulos, G. F. Giudice, and A. Romanino, "Aspects of split supersymmetry", *Nucl. Phys. B* **709** (2005) 3, doi:10.1016/j.nuclphysb.2004.12.026, arXiv:hep-ph/0409232.

[5] P. Gambino, G. F. Giudice, and P. Slavich, "Gluino decays in split supersymmetry", *Nucl. Phys. B* **726** (2005) 35, doi:10.1016/j.nuclphysb.2005.08.011, arXiv:hep-ph/0506214.

[6] A. Arvanitaki, N. Craig, S. Dimopoulos, and G. Villadoro, "Mini-split", *JHEP* **02** (2013) 126, doi:10.1007/JHEP02(2013)126, arXiv:1210.0555.

[7] N. Arkani-Hamed et al., "Simply unnatural supersymmetry", (2012). arXiv:1212.6971.

[8] P. Fayet, "Supergauge invariant extension of the Higgs mechanism and a model for the electron and its neutrino", *Nucl. Phys. B* **90** (1975) 104, doi:10.1016/0550-3213(75)90636-7.

[9] G. R. Farrar and P. Fayet, "Phenomenology of the production, decay, and detection of new hadronic states associated with supersymmetry", *Phys. Lett. B* **76** (1978) 575, doi:10.1016/0370-2693(78)90858-4.

[10] S. Weinberg, "Supersymmetry at ordinary energies. 1. masses and conservation laws", *Phys. Rev. D* **26** (1982) 287, doi:10.1103/PhysRevD.26.287.

[11] L. J. Hall and M. Suzuki, "Explicit *R*-parity breaking in supersymmetric models", *Nucl. Phys. B* **231** (1984) 419, doi:10.1016/0550-3213(84)90513-3.

[12] R. Barbier et al., "*R*-parity violating supersymmetry", *Phys. Rept.* **420** (2005) 1, doi:10.1016/j.physrep.2005.08.006, arXiv:hep-ph/0406039.

[13] G. F. Giudice and R. Rattazzi, "Theories with gauge mediated supersymmetry breaking", *Phys. Rept.* **322** (1999) 419, doi:10.1016/S0370-1573(99)00042-3, arXiv:hep-ph/9801271.

[14] P. Meade, N. Seiberg, and D. Shih, "General gauge mediation", *Prog. Theor. Phys. Suppl.* **177** (2009) 143, doi:10.1143/PTPS.177.143, arXiv:0801.3278.

[15] M. Buican, P. Meade, N. Seiberg, and D. Shih, "Exploring general gauge mediation", *JHEP* **03** (2009) 016, doi:10.1088/1126-6708/2009/03/016, arXiv:0812.3668.

[16] J. Fan, M. Reece, and J. T. Ruderman, "Stealth supersymmetry", *JHEP* **11** (2011) 012, doi:10.1007/JHEP11(2011)012, arXiv:1105.5135.

[17] J. Fan, M. Reece, and J. T. Ruderman, "A stealth supersymmetry sampler", *JHEP* **07** (2012) 196, doi:10.1007/JHEP07(2012)196, arXiv:1201.4875.

[18] M. J. Strassler and K. M. Zurek, "Echoes of a hidden valley at hadron colliders", *Phys. Lett. B* **651** (2007) 374, doi:10.1016/j.physletb.2007.06.055, arXiv:hep-ph/0604261.

[19] M. J. Strassler and K. M. Zurek, "Discovering the Higgs through highly-displaced vertices", *Phys. Lett. B* **661** (2008) 263, doi:10.1016/j.physletb.2008.02.008, arXiv:hep-ph/0605193.

[20] T. Han, Z. Si, K. M. Zurek, and M. J. Strassler, "Phenomenology of hidden valleys at hadron colliders", *JHEP* **07** (2008) 008, doi:10.1088/1126-6708/2008/07/008, arXiv:0712.2041.

[21] D. E. Kaplan, M. A. Luty, and K. M. Zurek, "Asymmetric dark matter", *Phys. Rev. D* **79** (2009) 115016, doi:10.1103/PhysRevD.79.115016, arXiv:0901.4117.

[22] L. J. Hall, K. Jedamzik, J. March-Russell, and S. M. West, "Freeze-in production of FIMP dark matter", *JHEP* **03** (2010) 080, doi:10.1007/JHEP03(2010)080, arXiv:0911.1120.

[23] I.-W. Kim and K. M. Zurek, "Flavor and collider signatures of asymmetric dark matter", *Phys. Rev. D* **89** (2014) 035008, doi:10.1103/PhysRevD.89.035008, arXiv:1310.2617.

[24] Y. Cui and B. Shuve, "Probing baryogenesis with displaced vertices at the LHC", *JHEP* **02** (2015) 049, doi:10.1007/JHEP02(2015)049, arXiv:1409.6729.

[25] R. T. Co, F. D'Eramo, L. J. Hall, and D. Pappadopulo, "Freeze-In dark matter with displaced signatures at colliders", *JCAP* **1512** (2015) 024, doi:10.1088/1475-7516/2015/12/024, arXiv:1506.07532.

[26] L. Calibbi, L. Lopez-Honorez, S. Lowette, and A. Mariotti, "Singlet-Doublet dark matter freeze-in: LHC displaced signatures versus cosmology", *JHEP* **09** (2018) 037, doi:10.1007/JHEP09(2018)037, arXiv:1805.04423.

[27] Y. Cui, L. Randall, and B. Shuve, "A WIMPy baryogenesis miracle", *JHEP* **04** (2012) 075, doi:10.1007/JHEP04(2012)075, arXiv:1112.2704.

[28] Y. Cui and R. Sundrum, "Baryogenesis for weakly interacting massive particles", *Phys. Rev. D* **87** (2013) 116013, doi:10.1103/PhysRevD.87.116013, arXiv:1212.2973.

[29] A. Atre, T. Han, S. Pascoli, and B. Zhang, "The search for heavy Majorana neutrinos", *JHEP* **05** (2009) 030, doi:10.1088/1126-6708/2009/05/030, arXiv:0901.3589.

[30] M. Drewes, "The phenomenology of right handed neutrinos", *Int. J. Mod. Phys. E* **22** (2013) 1330019, doi:10.1142/S0218301313300191, arXiv:1303.6912.

[31] F. F. Deppisch, P. S. Bhupal Dev, and A. Pilaftsis, "Neutrinos and collider physics", *New J. Phys.* **17** (2015) 075019, doi:10.1088/1367-2630/17/7/075019, arXiv:1502.06541.

[32] Y. Cai, T. Han, T. Li, and R. Ruiz, "Lepton Number Violation: Seesaw Models and Their Collider Tests", *Front. Phys.* **6** (2018) 40, doi:10.3389/fphy.2018.00040, arXiv:1711.02180.

[33] Z. Chacko, H.-S. Goh, and R. Harnik, "Natural electroweak breaking from a mirror symmetry", *Phys. Rev. Lett.* **96** (2006) 231802, doi:10.1103/PhysRevLett.96.231802, arXiv:hep-ph/0506256.

[34] H. Cai, H.-C. Cheng, and J. Terning, "A quirky little Higgs model", *JHEP* **05** (2009) 045, doi:10.1088/1126-6708/2009/05/045, arXiv:0812.0843.

[35] N. Craig, S. Knapen, and P. Longhi, "Neutral Naturalness from Orbifold Higgs Models", *Phys. Rev. Lett.* **114** (2015) 061803, doi:10.1103/PhysRevLett.114.061803, arXiv:1410.6808.

[36] N. Craig, A. Katz, M. Strassler, and R. Sundrum, "Naturalness in the dark at the LHC", *JHEP* **07** (2015) 105, doi:10.1007/JHEP07(2015)105, arXiv:1501.05310.

[37] D. Curtin and C. B. Verhaaren, "Discovering uncolored naturalness in exotic Higgs decays", *JHEP* **12** (2015) 072, doi:10.1007/JHEP12(2015)072, arXiv:1506.06141.

[38] CMS Collaboration, "The CMS experiment at the CERN LHC", *JINST* **3** (2008) S08004, doi:10.1088/1748-0221/3/08/S08004.

[39] CMS Collaboration, "Search for long-lived particles decaying into displaced jets in proton-proton collisions at $\sqrt{s} = 13$ TeV", *Phys. Rev. D* **99** (2019) 032011, doi:10.1103/PhysRevD.99.032011, arXiv:1811.07991.

[40] ATLAS Collaboration, "Search for long-lived, massive particles in events with displaced vertices and missing transverse momentum in $\sqrt{s}$ = 13 TeV pp collisions with the ATLAS detector", *Phys. Rev. D* **97** (2018) 052012, doi:10.1103/PhysRevD.97.052012, arXiv:1710.04901.

[41] ATLAS Collaboration, "Search for long-lived particles produced in pp collisions at $\sqrt{s} = 13$ TeV that decay into displaced hadronic jets in the ATLAS muon spectrometer", *Phys. Rev. D* **99** (2019) 052005, doi:10.1103/PhysRevD.99.052005, arXiv:1811.07370.

[42] ATLAS Collaboration, "Search for long-lived neutral particles in pp collisions at $\sqrt{s}$ = 13 TeV that decay into displaced hadronic jets in the ATLAS calorimeter", *Eur. Phys. J. C* **79** (2019) 481, doi:10.1140/epjc/s10052-019-6962-6, arXiv:1902.03094.

[43] ATLAS Collaboration, "Search for long-lived, massive particles in events with a displaced vertex and a muon with large impact parameter in pp collisions at $\sqrt{s} = 13$ TeV with the ATLAS detector", arXiv:2003.11956.

[44] ATLAS Collaboration, "Search for long-lived neutral particles produced in pp collisions at $\sqrt{s} = 13$ TeV decaying into displaced hadronic jets in the ATLAS inner detector and muon spectrometer", *Phys. Rev. D* **101** (2020) 052013, doi:10.1103/PhysRevD.101.052013, arXiv:1911.12575.

[45] CMS Collaboration, "Search for new long-lived particles at $\sqrt{s}$ = 13 TeV", *Phys. Lett. B* **780** (2018) 432, doi:10.1016/j.physletb.2018.03.019, arXiv:1711.09120.

[46] CMS Collaboration, "Search for long-lived particles with displaced vertices in multijet events in proton-proton collisions at $\sqrt{s}$ =13 TeV", *Phys. Rev. D* **98** (2018) 092011, doi:10.1103/PhysRevD.98.092011, arXiv:1808.03078.

[47] CMS Collaboration, "Search for long-lived particles using nonprompt jets and missing transverse momentum with proton-proton collisions at $\sqrt{s} = 13$ TeV", *Phys. Lett. B* **797** (2019) 134876, doi:10.1016/j.physletb.2019.134876, arXiv:1906.06441.

[48] CMS Collaboration, "The CMS trigger system", *JINST* **12** (2017) P01020, doi:10.1088/1748-0221/12/01/P01020, arXiv:1609.02366.

[49] M. Cacciari, G. P. Salam, and G. Soyez, "The anti-k_{T} jet clustering algorithm", *JHEP* **04** (2008) 063, doi:10.1088/1126-6708/2008/04/063, arXiv:0802.1189.

[50] M. Cacciari, G. P. Salam, and G. Soyez, "FastJet user manual", *Eur. Phys. J. C* **72** (2012) 1896, doi:10.1140/epjc/s10052-012-1896-2, arXiv:1111.6097.

[51] CMS Collaboration, "Jet energy scale and resolution in the CMS experiment in pp collisions at 8 TeV", *JINST* **12** (2017) P02014, doi:10.1088/1748-0221/12/02/P02014, arXiv:1607.03663.

[52] CMS Collaboration, "Technical proposal for the Phase-II upgrade of the CMS detector", CMS Technical proposal CERN-LHCC-2015-010, CMS-TDR-15-02, CERN, 2015.

[53] J. Alwall et al., "The automated computation of tree-level and next-to-leading order differential cross sections, and their matching to parton shower simulations", *JHEP* **07** (2014) 079, doi:10.1007/JHEP07(2014)079, arXiv:1405.0301.

[54] T. Sjöstrand et al., "An introduction to PYTHIA 8.2", *Comput. Phys. Commun.* **191** (2015) 159, doi:10.1016/j.cpc.2015.01.024, arXiv:1410.3012.

[55] J. Alwall et al., "Comparative study of various algorithms for the merging of parton showers and matrix elements in hadronic collisions", *Eur. Phys. J. C* **53** (2008) 473, doi:10.1140/epjc/s10052-007-0490-5, arXiv:0706.2569.

[56] CMS Collaboration, "Extraction and validation of a new set of CMS PYTHIA8 tunes from underlying-event measurements", *Eur. Phys. J. C* **80** (2020) 4, doi:10.1140/epjc/s10052-019-7499-4, arXiv:1903.12179.

[57] NNPDF Collaboration, "Parton distributions from high-precision collider data", *Eur. Phys. J. C* **77** (2017) 663, doi:10.1140/epjc/s10052-017-5199-5, arXiv:1706.00428.

[58] LHC Higgs Cross Section Working Group Collaboration, "Handbook of LHC Higgs cross sections: 4. Deciphering the nature of the Higgs sector", doi:10.23731/CYRM-2017-002, arXiv:1610.07922.

[59] G. Burdman, Z. Chacko, H.-S. Goh, and R. Harnik, "Folded supersymmetry and the LEP paradox", *JHEP* **02** (2007) 009, doi:10.1088/1126-6708/2007/02/009, arXiv:hep-ph/0609152.

[60] P. Nason, "A New method for combining NLO QCD with shower Monte Carlo algorithms", *JHEP* **11** (2004) 040, doi:10.1088/1126-6708/2004/11/040, arXiv:hep-ph/0409146.

[61] S. Frixione, P. Nason, and C. Oleari, "Matching NLO QCD computations with parton shower simulations: the POWHEG method", *JHEP* **11** (2007) 070, doi:10.1088/1126-6708/2007/11/070, arXiv:0709.2092.

[62] S. Alioli, P. Nason, C. Oleari, and E. Re, "A general framework for implementing NLO calculations in shower Monte Carlo programs: the POWHEG BOX", *JHEP* **06** (2010) 043, doi:10.1007/JHEP06(2010)043, arXiv:1002.2581.

[63] E. Bagnaschi, G. Degrassi, P. Slavich, and A. Vicini, "Higgs production via gluon fusion in the POWHEG approach in the SM and in the MSSM", *JHEP* **02** (2012) 088, doi:10.1007/JHEP02(2012)088, arXiv:1111.2854.

[64] Z. Liu and B. Tweedie, "The fate of long-lived superparticles with hadronic decays after LHC Run 1", *JHEP* **06** (2015) 042, doi:10.1007/JHEP06(2015)042, arXiv:1503.05923.

[65] C. Csaki, Y. Grossman, and B. Heidenreich, "Minimal flavor violation supersymmetry: a natural theory for *R*-parity violation", *Phys. Rev. D* **85** (2012) 095009, doi:10.1103/PhysRevD.85.095009, arXiv:1111.1239.

[66] P. W. Graham, D. E. Kaplan, S. Rajendran, and P. Saraswat, "Displaced supersymmetry", *JHEP* **07** (2012) 149, doi:10.1007/JHEP07(2012)149, arXiv:1204.6038.

[67] C. Csaki, E. Kuflik, and T. Volansky, "Dynamical *R*-parity violation", *Phys. Rev. Lett.* **112** (2014) 131801, doi:10.1103/PhysRevLett.112.131801, arXiv:1309.5957.

[68] C. Csaki, E. Kuflik, O. Slone, and T. Volansky, "Models of dynamical *R*-parity violation", *JHEP* **06** (2015) 045, doi:10.1007/JHEP06(2015)045, arXiv:1502.03096.

[69] C. Csaki et al., "Phenomenology of a long-lived LSP with R-parity violation", *JHEP* **08** (2015) 016, doi:10.1007/JHEP08(2015)016, arXiv:1505.00784.

[70] G. R. Farrar and P. Fayet, "Bounds on R-hadron production from calorimetry experiments", *Phys. Lett. B* **79** (1978) 442, doi:10.1016/0370-2693(78)90402-1.

[71] M. Fairbairn et al., "Stable massive particles at colliders", *Phys. Rept.* **438** (2007) 1, doi:10.1016/j.physrep.2006.10.002, arXiv:hep-ph/0611040.

[72] R. Mackeprang and A. Rizzi, "Interactions of coloured heavy stable particles in matter", *Eur. Phys. J. C* **50** (2007) 353, doi:10.1140/epjc/s10052-007-0252-4, arXiv:hep-ph/0612161.

[73] GEANT4 Collaboration, "GEANT4—a simulation toolkit", *Nucl. Instrum. Meth. A* **506** (2003) 250, doi:10.1016/S0168-9002(03)01368-8.

[74] CMS Collaboration, "Description and performance of track and primary-vertex reconstruction with the CMS tracker", *JINST* **9** (2014) P10009, doi:10.1088/1748-0221/9/10/P10009, arXiv:1405.6569.

[75] R. Frühwirth, W. Waltenberger, and P. Vanlaer, "Adaptive vertex fitting", *J. Phys. G* **34** (2007) N343, doi:10.1088/0954-3899/34/12/N01.

[76] CMS Collaboration, "Precision measurement of the structure of the CMS inner tracking system using nuclear interactions", *JINST* **13** (2018) P10034, doi:10.1088/1748-0221/13/10/P10034, arXiv:1807.03289.

[77] CMS Collaboration, "CMS technical design report for the pixel detector upgrade", Technical Report CERN-LHCC-2012-016, CMS-TDR-011, 2012. doi:10.2172/1151650.

[78] S. C. Johnson, "Hierarchical clustering schemes", *Psychometrika* **32** (1967) 241, doi:10.1007/BF02289588.

[79] Y. Freund and R. E. Schapire, "Experiments with a new boosting algorithm", in *Proceedings of the Thirteenth International Conference on International Conference on Machine Learning*, ICML'96, p. 148. Morgan Kaufmann Publishers Inc., San Francisco, CA, USA, 1996.

[80] J. Friedman, T. Hastie, and R. Tibshirani, "Additive logistic regression: a statistical view of boosting (with discussion and a rejoinder by the authors)", *Ann. Statist.* **28** (2000) 337, doi:10.1214/aos/1016218223.

[81] J. H. Friedman, "Greedy function approximation: A gradient boosting machine.", *Ann. Statist.* **29** (2001) 1189, doi:10.1214/aos/1013203451.

[82] H. Voss, A. Höcker, J. Stelzer, and F. Tegenfeldt, "TMVA, the toolkit for multivariate data analysis with ROOT", in *XIth International Workshop on Advanced Computing and Analysis Techniques in Physics Research (ACAT)*, p. 40. 2007. arXiv:physics/0703039. [PoS(ACAT)040]. doi:10.22323/1.050.0040.

[83] F. Pedregosa et al., "Scikit-learn: Machine learning in Python", *J. Mach. Learn. Res.* **12** (2011) 2825.

[84] CMS Collaboration, "CMS luminosity measurement for the 2017 data-taking period at $\sqrt{s} = 13$ TeV", CMS Physics Analysis Summary CMS-PAS-LUM-17-004, 2018.

[85] CMS Collaboration, "CMS luminosity measurement for the 2018 data-taking period at $\sqrt{s} = 13$ TeV", CMS Physics Analysis Summary CMS-PAS-LUM-18-002, 2019.

[86] S. Dulat et al., "New parton distribution functions from a global analysis of quantum chromodynamics", *Phys. Rev. D* **93** (2016) 033006, doi:10.1103/PhysRevD.93.033006, arXiv:1506.07443.

[87] L. A. Harland-Lang, A. D. Martin, P. Motylinski, and R. S. Thorne, "Parton distributions in the LHC era: MMHT 2014 PDFs", *Eur. Phys. J. C* **75** (2015) 204, doi:10.1140/epjc/s10052-015-3397-6, arXiv:1412.3989.

[88] J. Butterworth et al., "PDF4LHC recommendations for LHC Run II", *J. Phys. G* **43** (2016) 023001, doi:10.1088/0954-3899/43/2/023001, arXiv:1510.03865.

[89] A. Buckley et al., "LHAPDF6: parton density access in the LHC precision era", *Eur. Phys. J. C* **75** (2015) 132, doi:10.1140/epjc/s10052-015-3318-8, arXiv:1412.7420.

[90] T. Junk, "Confidence level computation for combining searches with small statistics", *Nucl. Instrum. Meth. A* **434** (1999) 435, doi:10.1016/S0168-9002(99)00498-2, arXiv:hep-ex/9902006.

[91] A. L. Read, "Presentation of search results: The CL_s technique", *J. Phys. G* **28** (2002) 2693, doi:10.1088/0954-3899/28/10/313.

[92] G. Cowan, K. Cranmer, E. Gross, and O. Vitells, "Asymptotic formulae for likelihood-based tests of new physics", *Eur. Phys. J. C* **71** (2011) 1554, doi:10.1140/epjc/s10052-011-1554-0, arXiv:1007.1727. [Erratum: doi:10.1140/epjc/s10052-013-2501-z].

[93] The ATLAS Collaboration, The CMS Collaboration, The LHC Higgs Combination Group, "Procedure for the LHC Higgs boson search combination in Summer 2011", Technical Report CMS-NOTE-2011-005, ATL-PHYS-PUB-2011-11, 2011.

[94] W. Beenakker, R. Hopker, M. Spira, and P. M. Zerwas, "Squark and gluino production at hadron colliders", *Nucl. Phys. B* **492** (1997) 51, doi:10.1016/S0550-3213(97)80027-2, arXiv:hep-ph/9610490.

[95] A. Kulesza and L. Motyka, "Threshold resummation for squark-antisquark and gluino-pair production at the LHC", *Phys. Rev. Lett.* **102** (2009) 111802, doi:10.1103/PhysRevLett.102.111802, arXiv:0807.2405.

[96] A. Kulesza and L. Motyka, "Soft gluon resummation for the production of gluino-gluino and squark-antisquark pairs at the LHC", *Phys. Rev. D* **80** (2009) 095004, doi:10.1103/PhysRevD.80.095004, arXiv:0905.4749.

[97] W. Beenakker et al., "Squark and gluino hadroproduction", *Int. J. Mod. Phys. A* **26** (2011) 2637, doi:10.1142/S0217751X11053560, arXiv:1105.1110.

[98] C. Borschensky et al., "Squark and gluino production cross sections in pp collisions at $\sqrt{s}$ = 13, 14, 33 and 100 TeV", *Eur. Phys. J. C* **74** (2014) 3174, doi:10.1140/epjc/s10052-014-3174-y, arXiv:1407.5066.

[99] W. Beenakker et al., "NNLL-fast: predictions for coloured supersymmetric particle production at the LHC with threshold and Coulomb resummation", *JHEP* **12** (2016) 133, doi:10.1007/JHEP12(2016)133, arXiv:1607.07741.

A Supplemental information

Table 5: Signal efficiencies (in %) for the jet-jet model in 2017 and 2018 at different proper decay lengths $c\tau_0$ and different masses m_X. Selection requirements are cumulative from the first row to the last. Uncertainties are statistical only.

Efficiency (%)	m_X (GeV)	$c\tau_0$ 1 mm	10 mm	30 mm	100 mm	1000 mm
Trigger	1000	29.47 ± 0.38	89.98 ± 0.67	91.16 ± 0.68	84.41 ± 0.65	71.72 ± 0.66
Preselection		22.56 ± 0.34	85.22 ± 0.65	84.92 ± 0.65	73.83 ± 0.61	27.47 ± 0.41
Final selection		16.27 ± 0.29	73.63 ± 0.61	73.51 ± 0.61	61.51 ± 0.55	20.13 ± 0.35
Trigger	300	25.05 ± 0.35	70.50 ± 0.59	68.19 ± 0.58	58.97 ± 0.54	30.22 ± 0.39
Preselection		17.42 ± 0.30	59.89 ± 0.55	55.40 ± 0.53	42.38 ± 0.46	9.11 ± 0.21
Final selection		12.06 ± 0.25	48.41 ± 0.49	45.13 ± 0.48	32.42 ± 0.40	5.87 ± 0.17
Trigger	100	2.65 ± 0.12	6.97 ± 0.19	6.47 ± 0.18	4.87 ± 0.16	0.95 ± 0.07
Preselection		1.81 ± 0.10	4.94 ± 0.16	4.41 ± 0.15	2.59 ± 0.11	0.28 ± 0.04
Final selection		1.03 ± 0.07	3.47 ± 0.13	3.00 ± 0.12	1.64 ± 0.09	0.17 ± 0.03

Table 6: Signal efficiencies (in 10^{-4}) for the model where the SM Higgs boson decays to two long-lived scalars S in 2017 and 2018 at different proper decay lengths $c\tau_0$ and with $m_S = 55$ GeV. The long-lived scalars is assumed to decay to a down quark-antiquark pair ($S \to d\bar{d}$). Selection requirements are cumulative from the first row to the last. Uncertainties are statistical only.

Efficiency ($\times 10^{-4}$)	m_S (GeV)	$c\tau_0$ 1 mm	10 mm	30 mm	100 mm	1000 mm
Trigger	55	6.63 ± 0.13	32.07 ± 0.29	33.44 ± 1.16	25.25 ± 0.26	5.71 ± 0.12
Preselection		3.11 ± 0.09	13.61 ± 1.89	13.72 ± 0.75	9.39 ± 0.16	1.36 ± 0.06
Final selection		0.95 ± 0.05	6.12 ± 0.13	6.34 ± 0.42	4.46 ± 0.11	0.64 ± 0.04

Table 7: Signal efficiencies (in 10^{-4}) for the model where the SM Higgs boson decays to two long-lived scalars S in 2017 and 2018 at different proper decay lengths $c\tau_0$ and with $m_S = 55$ GeV. The long-lived scalar is assumed to decay to a bottom quark-antiquark pair ($S \to b\bar{b}$). Selection requirements are cumulative from the first row to the last. Uncertainties are statistical only.

Efficiency ($\times 10^{-4}$)	m_S (GeV)	$c\tau_0$ 1 mm	10 mm	30 mm	100 mm	1000 mm
Trigger	55	4.30 ± 0.11	22.56 ± 0.24	24.45 ± 0.48	17.78 ± 0.21	4.05 ± 0.10
Preselection		0.66 ± 0.04	3.30 ± 0.09	3.97 ± 0.19	3.37 ± 0.09	0.57 ± 0.04
Final selection		0.08 ± 0.01	0.96 ± 0.05	1.17 ± 0.10	1.09 ± 0.05	0.19 ± 0.02

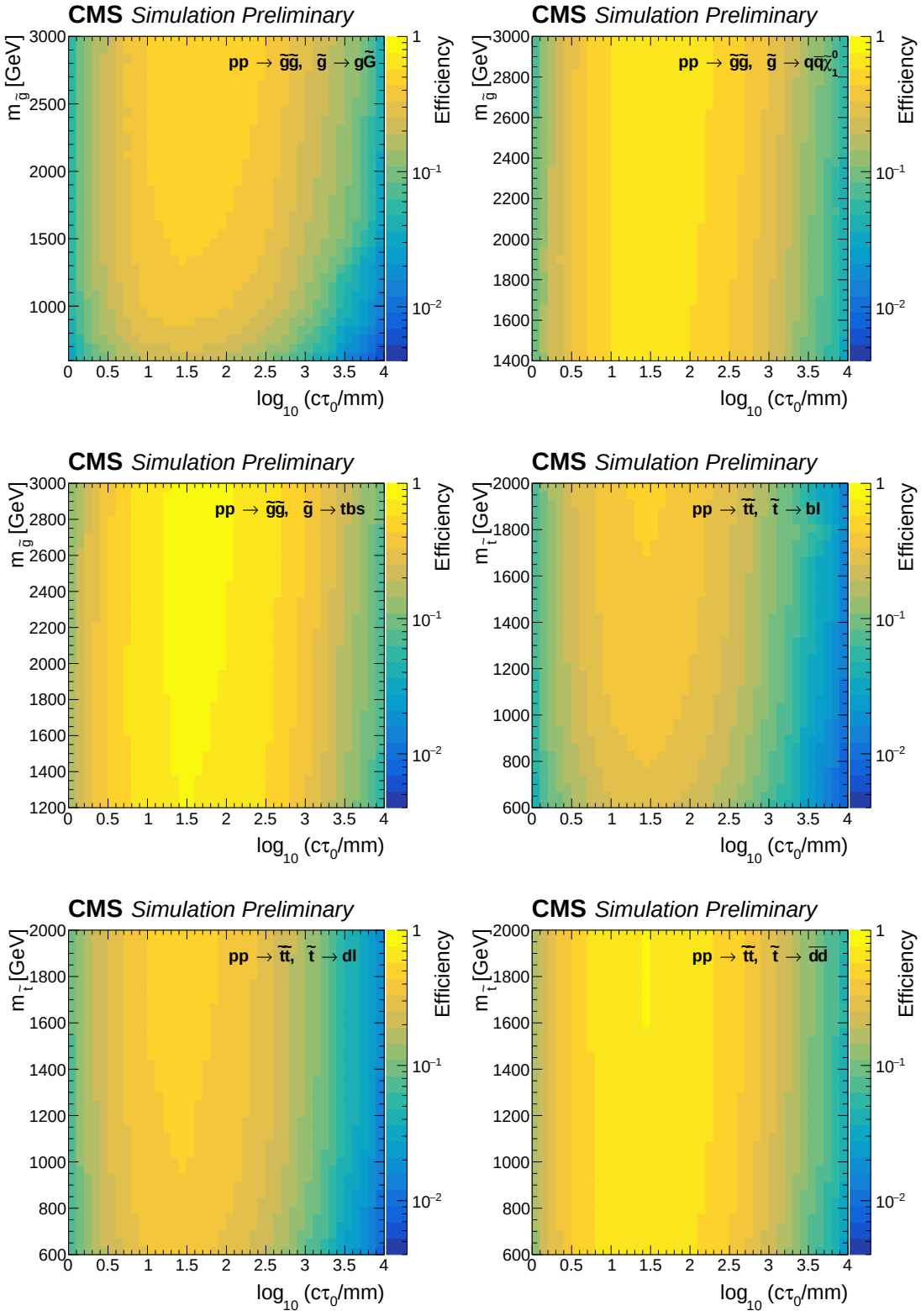

Figure 15: The signal efficiencies as functions of the long-lived particle mass and mean proper decay lengths in 2017 and 2018, for $\widetilde{g} \to g\widetilde{G}$ model (top left), $\widetilde{g} \to q\bar{q}\widetilde{\chi}_1^0$ model (top right), $\widetilde{g} \to tbs$ model (middle left), $\widetilde{t} \to b\ell$ model (middle right), $\widetilde{t} \to d\ell$ model (bottom left), and $\widetilde{t} \to d\bar{d}$ model (bottom right).

Table 8: Signal efficiencies (in %) for the $\widetilde{g} \to g\widetilde{G}$ model in 2017 and 2018 at different proper decay lengths $c\tau_0$ and different masses $m_{\widetilde{g}}$. Selection requirements are cumulative from the first row to the last. Uncertainties are statistical only.

Efficiency (%)	$m_{\widetilde{g}}$ (GeV)	$c\tau_0$ 1 mm	10 mm	30 mm	100 mm	1000 mm
Trigger		10.69 ± 0.24	69.70 ± 0.60	81.86 ± 0.65	82.86 ± 0.66	73.07 ± 0.38
Preselection	2400	7.03 ± 0.19	63.62 ± 0.57	72.80 ± 0.61	69.67 ± 0.60	35.54 ± 0.27
Final selection		3.84 ± 0.14	44.20 ± 0.48	52.69 ± 0.52	50.84 ± 0.52	24.19 ± 0.22
Trigger		12.04 ± 0.25	68.36 ± 0.59	79.64 ± 0.64	79.96 ± 0.64	67.49 ± 0.38
Preselection	1600	7.52 ± 0.20	60.55 ± 0.56	68.74 ± 0.59	63.47 ± 0.57	29.57 ± 0.25
Final selection		4.02 ± 0.15	41.33 ± 0.46	47.67 ± 0.49	43.16 ± 0.47	19.53 ± 0.20
Trigger		12.14 ± 0.25	62.77 ± 0.56	72.44 ± 0.60	71.90 ± 0.60	52.77 ± 0.51
Preselection	1000	7.29 ± 0.19	53.19 ± 0.52	57.56 ± 0.54	52.25 ± 0.51	21.10 ± 0.32
Final selection		3.75 ± 0.14	34.57 ± 0.42	37.55 ± 0.43	33.84 ± 0.41	12.88 ± 0.25

Table 9: Signal efficiencies (in %) for the $\widetilde{g} \to q\bar{q}\widetilde{\chi}_1^0$ model ($m_{\widetilde{\chi}_1^0} = 100$ GeV) in 2017 and 2018 at different proper decay lengths $c\tau_0$ and different masses $m_{\widetilde{g}}$. Selection requirements are cumulative from the first row to the last. Uncertainties are statistical only.

Efficiency (%)	$m_{\widetilde{g}}$ (GeV)	$c\tau_0$ 1 mm	10 mm	30 mm	100 mm	1000 mm
Trigger		15.08 ± 0.28	82.32 ± 0.66	90.46 ± 0.69	87.65 ± 0.68	78.78 ± 0.65
Preselection	2600	9.91 ± 0.23	77.60 ± 0.64	85.82 ± 0.67	80.22 ± 0.65	43.24 ± 0.48
Final selection		5.75 ± 0.17	59.12 ± 0.56	68.44 ± 0.60	63.26 ± 0.58	30.84 ± 0.41
Trigger		17.70 ± 0.31	83.21 ± 0.67	90.46 ± 0.69	87.66 ± 0.68	79.04 ± 0.65
Preselection	2000	11.20 ± 0.24	77.74 ± 0.65	85.04 ± 0.67	79.45 ± 0.65	39.69 ± 0.46
Final selection		6.57 ± 0.19	58.36 ± 0.56	66.29 ± 0.59	60.96 ± 0.57	27.12 ± 0.38
Trigger		19.39 ± 0.32	82.56 ± 0.66	90.27 ± 0.69	87.70 ± 0.68	78.31 ± 0.64
Preselection	1600	12.16 ± 0.26	76.59 ± 0.64	84.13 ± 0.59	77.71 ± 0.64	37.41 ± 0.44
Final selection		6.76 ± 0.19	57.19 ± 0.55	64.37 ± 0.58	57.98 ± 0.55	25.02 ± 0.36

Table 10: Signal efficiencies (in %) for the $\widetilde{g} \to tbs$ model in 2017 and 2018 at different proper decay lengths $c\tau_0$ and different masses $m_{\widetilde{g}}$. Selection requirements are cumulative from the first row to the last. Uncertainties are statistical only.

Efficiency (%)	$m_{\widetilde{g}}$ (GeV)	$c\tau_0$ 1 mm	10 mm	30 mm	100 mm	1000 mm
Trigger		25.14 ± 0.39	90.65 ± 0.70	95.78 ± 0.73	91.42 ± 0.73	83.61 ± 0.67
Preselection	2600	16.26 ± 0.31	87.43 ± 0.69	94.08 ± 0.73	89.30 ± 0.72	56.49 ± 0.55
Final selection		9.60 ± 0.24	71.09 ± 0.62	81.12 ± 0.67	77.55 ± 0.67	42.62 ± 0.48
Trigger		29.89 ± 0.42	91.95 ± 0.71	95.53 ± 0.73	91.58 ± 0.72	83.38 ± 0.68
Preselection	2000	18.93 ± 0.34	88.27 ± 0.70	93.55 ± 0.72	89.17 ± 0.71	52.54 ± 0.54
Final selection		11.29 ± 0.26	72.14 ± 0.63	79.58 ± 0.67	75.52 ± 0.65	38.12 ± 0.46
Trigger		31.61 ± 0.43	92.16 ± 0.71	95.58 ± 0.76	92.03 ± 0.72	84.50 ± 0.67
Preselection	1600	20.06 ± 0.34	88.40 ± 0.70	93.46 ± 0.75	89.04 ± 0.71	50.46 ± 0.52
Final selection		11.71 ± 0.26	70.85 ± 0.63	78.52 ± 0.69	73.77 ± 0.65	35.91 ± 0.44

Table 11: Signal efficiencies (in %) for the $\widetilde{t} \to b\ell$ model at different proper decay lengths $c\tau_0$ and different masses $m_{\widetilde{t}}$. Selection requirements are cumulative from the first row to the last. Uncertainties are statistical only.

Efficiency (%)	$m_{\widetilde{t}}$ (GeV)	$c\tau_0$				
		1 mm	10 mm	30 mm	100 mm	1000 mm
Trigger		18.00 ± 0.30	66.30 ± 0.58	74.36 ± 0.62	74.48 ± 0.62	66.67 ± 0.59
Preselection	1600	8.45 ± 0.21	54.41 ± 0.53	59.13 ± 0.56	52.63 ± 0.52	21.00 ± 0.33
Final selection		5.03 ± 0.16	39.77 ± 0.45	42.85 ± 0.48	37.02 ± 0.44	12.58 ± 0.25
Trigger		20.13 ± 0.32	65.37 ± 0.58	73.13 ± 0.61	73.74 ± 0.61	61.20 ± 0.56
Preselection	1000	8.32 ± 0.21	48.92 ± 0.49	53.45 ± 0.53	47.68 ± 0.49	16.99 ± 0.30
Final selection		4.65 ± 0.16	33.46 ± 0.41	37.56 ± 0.44	31.81 ± 0.40	10.12 ± 0.23
Trigger		19.96 ± 0.32	58.90 ± 0.54	64.58 ± 0.58	64.93 ± 0.58	48.32 ± 0.50
Preselection	600	6.85 ± 0.19	39.15 ± 0.44	42.25 ± 0.47	36.80 ± 0.44	11.59 ± 0.25
Final selection		3.33 ± 0.13	24.44 ± 0.35	27.69 ± 0.38	23.12 ± 0.35	6.47 ± 0.18

Table 12: Signal efficiencies (in %) for the $\widetilde{t} \to d\ell$ model in 2017 and 2018 at different proper decay lengths $c\tau_0$ and different masses $m_{\widetilde{t}}$. Selection requirements are cumulative from the first row to the last. Uncertainties are statistical only.

Efficiency (%)	$m_{\widetilde{t}}$ (GeV)	$c\tau_0$				
		1 mm	10 mm	30 mm	100 mm	1000 mm
Trigger		18.58 ± 0.31	66.73 ± 0.59	74.69 ± 0.63	74.59 ± 0.64	67.27 ± 0.60
Preselection	1600	10.72 ± 0.24	57.96 ± 0.55	63.08 ± 0.58	56.77 ± 0.56	22.79 ± 0.35
Final selection		6.62 ± 0.19	43.88 ± 0.48	47.92 ± 0.51	41.09 ± 0.47	14.33 ± 0.28
Trigger		19.95 ± 0.33	66.23 ± 0.59	73.87 ± 0.63	73.99 ± 0.64	62.66 ± 0.57
Preselection	1000	9.71 ± 0.23	55.31 ± 0.54	59.93 ± 0.57	53.79 ± 0.54	19.80 ± 0.32
Final selection		5.60 ± 0.17	41.22 ± 0.47	44.38 ± 0.49	38.07 ± 0.46	12.34 ± 0.25
Trigger		20.27 ± 0.33	60.49 ± 0.58	66.86 ± 0.61	66.85 ± 0.61	49.73 ± 0.52
Preselection	600	8.83 ± 0.22	47.48 ± 0.51	50.55 ± 0.53	44.37 ± 0.50	13.46 ± 0.27
Final selection		5.14 ± 0.17	33.96 ± 0.43	36.03 ± 0.45	30.16 ± 0.41	8.19 ± 0.21

Table 13: Signal efficiencies (in %) for the $\widetilde{t} \to \overline{d}\,\overline{d}$ model in 2017 and 2018 at different proper decay lengths $c\tau_0$ and different masses $m_{\widetilde{t}}$. Selection requirements are cumulative from the first row to the last. Uncertainties are statistical only.

Efficiency (%)	$m_{\widetilde{t}}$ (GeV)	$c\tau_0$				
		1 mm	10 mm	30 mm	100 mm	1000 mm
Trigger		22.10 ± 0.35	87.15 ± 0.71	92.19 ± 0.72	87.73 ± 0.71	79.12 ± 0.67
Preselection	1600	17.06 ± 0.31	84.06 ± 0.70	88.49 ± 0.71	81.10 ± 0.68	39.89 ± 0.48
Final selection		11.78 ± 0.26	71.44 ± 0.65	76.02 ± 0.66	67.02 ± 0.62	28.52 ± 0.40
Trigger		23.86 ± 0.36	86.99 ± 0.72	91.58 ± 0.77	88.19 ± 0.70	78.31 ± 0.66
Preselection	1000	16.96 ± 0.30	82.33 ± 0.70	86.73 ± 0.75	79.72 ± 0.67	35.91 ± 0.45
Final selection		11.91 ± 0.26	69.01 ± 0.64	73.52 ± 0.69	64.23 ± 0.60	25.52 ± 0.38
Trigger		24.51 ± 0.37	84.75 ± 0.68	89.27 ± 0.70	85.55 ± 0.68	69.66 ± 0.61
Preselection	600	15.80 ± 0.29	78.05 ± 0.66	81.84 ± 0.67	74.51 ± 0.64	29.37 ± 0.39
Final selection		11.15 ± 0.25	64.32 ± 0.60	67.68 ± 0.61	58.85 ± 0.57	20.66 ± 0.33